

van Hove, Rashba, and Hubbard meet to form first-order and higher-order topological superconductors

Pietro M. Bonetti,^{1,*} Debmalya Chakraborty,^{2,*} Xianxin Wu,³ and Andreas P. Schnyder^{1,4}

¹*Max Planck Institute for Solid State Research, Heisenbergstrasse 1, D-70569 Stuttgart, Germany*

²*Department of Physics and Astronomy, Uppsala University, Box 516, S-751 20 Uppsala, Sweden*

³*Institute for Theoretical Physics, Chinese Academy of Sciences, Beijing, China*

⁴*Yukawa Institute for Theoretical Physics (YITP), Kyoto University, Kyoto 606-8502, Japan*

(Dated: April 17, 2023)

We investigate topological superconductivity in the Rashba-Hubbard model, describing heavy-atom superlattice and van der Waals materials with broken inversion. We focus in particular on fillings close to the van Hove singularities, where a large density of states enhances the superconducting transition temperature. To determine the topology of the superconducting gaps and to analyze the stability of their surface states in the presence of disorder and residual interactions, we develop an fRG+MFT approach, which combines the unbiased functional renormalization group (fRG) with a real-space mean-field theory (MFT). Our approach uncovers a cascade of topological superconducting states, including A_1 and B_1 pairings, whose wave functions are of dominant p - and d -wave character, respectively, as well as a time-reversal breaking $A_1 + iB_1$ pairing. While the A_1 and B_1 states have first order topology with helical and flat-band Majorana states, respectively, the $A_1 + iB_1$ pairing exhibits second-order topology with Majorana corner modes. Implications for experimental systems and potential applications for quantum technologies are being discussed.

Topological superconductors (TSCs) are of high current interest due to their exceptional properties and potential for applications in quantum information technologies [1–7]. There are two different types of TSCs: (i) Engineered heterostructures in which topological superconductivity is proximity induced by a conventional s -wave superconductor and (ii) intrinsic TSCs which arise as an intrinsic property of the material. While a great variety of different heterostructures realizing TSCs has been proposed [7], progress in the field of intrinsic TSCs has been less swift. One of the most promising recent examples of intrinsic TSCs are perhaps the iron-based superconductors [8, 9], in which evidence for zero-energy vortex bound states of topological origin has been reported [10, 11]. Intrinsic TSCs have several advantages compared to their engineered counterparts: For one, they exhibit higher transition temperatures and are less affected by impurities. Moreover, their topological superconductivity exists in the entire volume of the material, and not just at a heterostructure interface.

With the recent progress in the MBE synthesis of superlattices [12] and in the fabrication of 2D van der Waals materials [13–15], the design of intrinsic TSCs is now becoming a reality. Particularly promising are van der Waals heavy-atom materials [16–18] and heavy-atom superlattices, such as LAO/STO [19, 20], EuO/KTO [21], and CeCoIn₅/YbCoIn₅ [22, 23]. The latter shows signs of unconventional superconductivity below the relatively high transition temperature $T_c \simeq 2$ K. An important feature of these designer materials is their high tunability. For example, the Rashba spin-orbit coupling in the CeCoIn₅/YbCoIn₅ superlattices can be adjusted by the

width of the YbCoIn₅ blocks. In light of these recent developments, it is now becoming paramount to investigate which types of Fermi surface shapes and spin-orbit couplings are conducive for topological superconductivity at large T_c .

Motivated by this, we theoretically analyze the conditions under which topological superconductivity emerges in the Rashba-Hubbard model [24–31], which captures the electronic correlation physics of the above mentioned 2D heavy-atom materials. Focusing on the t - t' square lattice with nearest-neighbor Rashba spin-orbit coupling, we investigate the superconducting pairing propensity as a function of t' and hole doping. We are in particular interested in the pairing states near the van Hove fillings, since there a large density of states enhances T_c . Due to the mutual interference between particle-particle and particle-hole instabilities at the van Hove singularities, an unbiased numerical method is required to reliably determine the superconducting pairing states. We therefore employ the truncated-unity functional renormalization group (fRG) [32, 33], which treats all instability channels on an equal footing. In order to investigate the topological characteristics as well as the edge and disorder properties of the dominant pairing states, we introduce here, in addition, a novel fRG+MFT approach, which combines the fRG analysis with a real-space mean-field theory (MFT) calculation [34–37]. Within this framework, we are able to deduce in an impartial manner not only the pairing symmetries, but also the topological and edge properties of the superconducting states, as well as the (in-)stabilities of the edge states against residual interactions. This allows us to quantitatively predict the topological superconducting features of the Rashba-Hubbard model, which in turn informs the design of superconducting 2D van der Waals and superlattice materials with nontrivial topology.

* These two authors contributed equally

Specifically, we find that ferro- and antiferromagnetic fluctuations, which are strongly enhanced near the van Hove singularities, lead to A_1 and B_1 superconducting states, with dominant p - and d -wave like pairing character, respectively, and a T_c estimated to be as high as $\sim 10^{-2}t$ for $U = 3t$. Both of these pairing states exhibit nontrivial first order topology [3] and host helical and flat-band Majorana edge states, respectively. Remarkably, we find near the phase boundary between these two states in addition a time-reversal breaking $A_1 + iB_1$ pairing state with higher-order topology and Majorana corner modes [38–46]. Our combined fRG+MFT approach reveals that while both the helical Majorana and corner edge states are robust to residual interactions, the flat-band Majorana states are unstable towards the formation of a 1D phase crystal [47–49]. Our findings provide a route towards the design of intrinsic topological superconductors with potential applications in quantum information technologies [50, 51].

Results

Before analyzing the different pairing instabilities in detail, we first briefly describe the model Hamiltonian and the employed fRG + MFT approach.

Model and methods. We start from the Rashba-Hubbard Hamiltonian on the square lattice (with lattice spacing $a = 1$) given by $H = H_0 + H_U$, with

$$H_0 = \sum_{j,j',\sigma} t_{jj'} c_{j,\sigma}^\dagger c_{j',\sigma} - \mu \sum_{j,\sigma} n_{j,\sigma} + i \sum_{j,j',\sigma,\sigma'} \lambda_{jj'} \left[(\mathbf{r}_j - \mathbf{r}_{j'}) \times c_{j,\sigma}^\dagger \vec{\tau}_{\sigma\sigma'} c_{j',\sigma'} \right]_z + \text{H.c.}, \quad (1)$$

$$H_U = U \sum_j n_{j,\uparrow} n_{j,\downarrow},$$

where $c_{j,\sigma}$ ($c_{j,\sigma}^\dagger$) is the annihilation (creation) operator of an electron at site j with spin projection σ , $\vec{\tau}$ are the Pauli matrices, \mathbf{r}_j is the lattice coordinate of site j , $n_{j,\sigma} = c_{j,\sigma}^\dagger c_{j,\sigma}$ is the spin-resolved particle number operator, μ is the chemical potential, H_0 is the non-interacting part and H_U is the Hubbard interaction term. Hamiltonian (1) is described by few parameters: the hopping amplitudes $t_{jj'}$, the Rashba couplings $\lambda_{jj'}$, and the onsite Hubbard repulsive interaction $U > 0$. In the following, we choose the hopping amplitudes such that $t_{\langle j,j' \rangle} = -t$ when j and j' are nearest neighbors, $t_{\langle\langle j,j' \rangle\rangle} = -t'$ when j and j' are second neighbors, and zero otherwise. We also consider the Rashba spin-orbit coupling to be nonzero only for nearest neighbors $\lambda_{\langle j,j' \rangle} = \lambda t$. Fourier transforming the quadratic part of the Hamiltonian, one obtains

$$H_0 = \int_{\mathbf{k}} c_{\mathbf{k}}^\dagger \hat{\mathcal{H}}_{\mathbf{k}} c_{\mathbf{k}}, \quad (2)$$

where $\int_{\mathbf{k}} = \int_{\text{BZ}} \frac{d^2 k}{(2\pi)^2}$ is a shorthand for the integral over the first Brillouin zone. $\hat{\mathcal{H}}_{\mathbf{k}}$ is a 2×2 matrix that reads

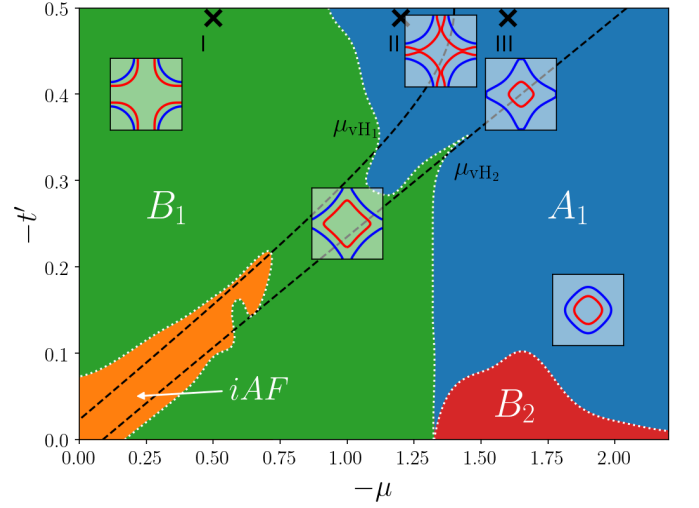


Figure 1. **Superconducting phase diagram.** Phase diagram of the Rashba-Hubbard model on the square lattice as a function of chemical potential μ and second-neighbor hopping t' for $U = 3t$. t' and μ are measured in units of the nearest-neighbor hopping amplitude t . The dashed lines indicate the values of the chemical potential $\mu_{vH_1}(t')$, $\mu_{vH_2}(t')$ where the van Hove singularities VHS1 and VHS2 occur.

as

$$\hat{\mathcal{H}}_{\mathbf{k}} = (\epsilon_{\mathbf{k}} - \mu) \mathbb{1} + \lambda \vec{g}_{\mathbf{k}} \cdot \vec{\tau}, \quad (3)$$

with $\epsilon_{\mathbf{k}} = -2t(\cos k_x + \cos k_y) - 4t' \cos k_x \cos k_y$ the Fourier transform of $t_{jj'}$, and $\vec{g}_{\mathbf{k}} = 2t(-\sin k_y, \sin k_x, 0)$. Hamiltonian (3) can be easily diagonalized introducing the so-called *helicity basis*, $c_{\mathbf{k}} \rightarrow U_{\mathbf{k}} c_{\mathbf{k}}$, with

$$U_{\mathbf{k}} = \frac{1}{\sqrt{2}} \begin{pmatrix} 1 & e^{-i\phi_{\mathbf{k}}} \\ -e^{i\phi_{\mathbf{k}}} & 1 \end{pmatrix}, \quad (4)$$

with $e^{i\phi_{\mathbf{k}}} = (g_{1,\mathbf{k}} + ig_{2,\mathbf{k}})/|\vec{g}_{\mathbf{k}}|$, leading to the quasiparticle bands $E_{\mathbf{k}}^{\pm} = \epsilon_{\mathbf{k}} - \mu \pm \lambda |\vec{g}_{\mathbf{k}}|$. Model (1) explicitly breaks parity (inversion) symmetry, hence its superconducting states cannot be classified as even-parity (spin-singlet) or odd-parity (spin-triplet). Rather, they are a superposition of the two.

We investigate the superconducting (SC) phases of the model in Eq. (1) by means of the functional renormalization (fRG) group, combined with mean-field theory (fRG+MFT) [34–37]. This results in a renormalized superconducting gap equation of the form

$$\Delta_{\mathbf{k}}^{\sigma\sigma'} = \sum_{s,s'} \int_{\mathbf{k}'} \tilde{V}_{\mathbf{k}\mathbf{k}'}^{\sigma\sigma's's'} \left[T \sum_n F^{ss'}(\mathbf{k}', \nu_n) \right], \quad (5)$$

where ν_n are fermionic Matsubara frequencies, T is the temperature, $\Delta_{\mathbf{k}}^{\sigma\sigma'}$ is the SC order parameter, and $F^{ss'}(\mathbf{k}', \nu_n)$ is the spin-resolved anomalous propagator, describing the propagation of a hole that gets reflected into a particle or vice-versa. The function $\tilde{V}_{\mathbf{k}\mathbf{k}'}^{\sigma\sigma's's'}$ describes an effective interaction, computed by means of

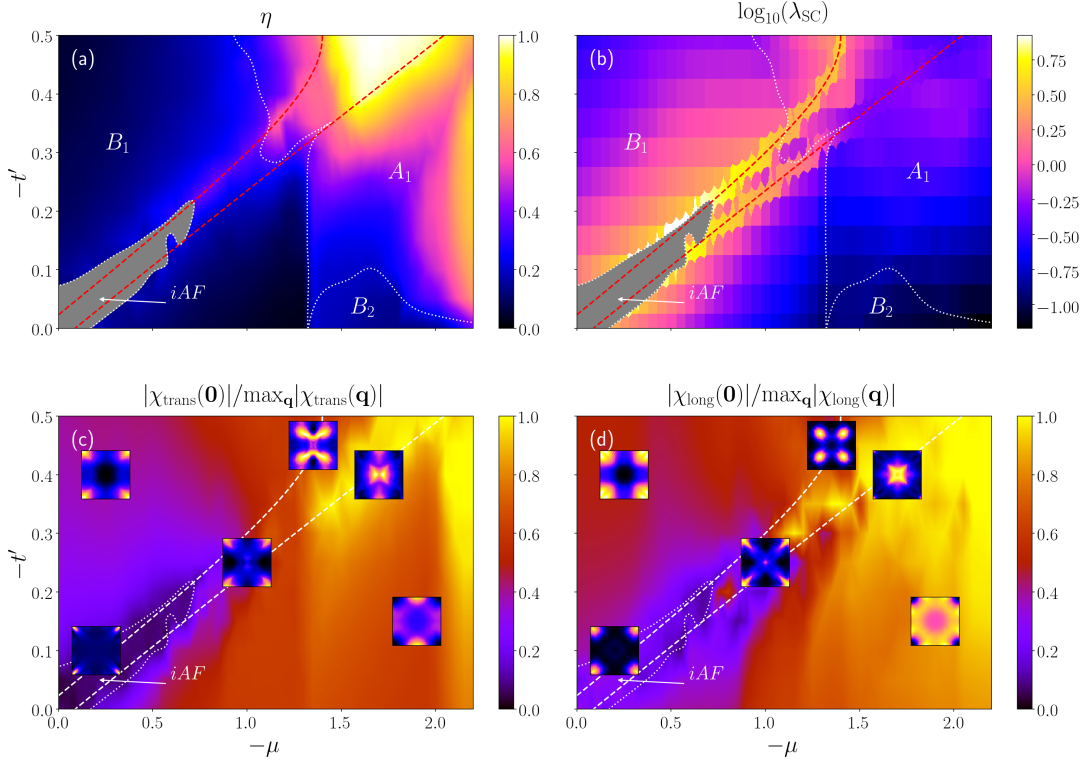


Figure 2. **Triplet-to-singlet ratio and ferromagnetic fluctuations.** Panel (a): triplet strength η of the superconducting state as a function of chemical potential μ and second-neighbor hopping t' . Panel (b): leading superconducting eigenvalue λ_{SC} computed at $T = 10^{-6}t$. Panels (c) and (d): ferromagnetic fluctuations in (c) the transverse and (d) the longitudinal spin susceptibility. The insets are colormaps of the momentum dependence of the relative susceptibility.

the fRG (see Methods Section and Supplementary Information SI for a deeper explanation). To determine the symmetry (and not the size) of the SC gap, we linearize Eq. (5) in $\Delta_{\mathbf{k}}^{\sigma\sigma'}$. The equation becomes therefore an eigenvalue problem, where the eigenvector corresponding to the largest positive eigenvalue gives the information on the symmetry of the leading superconducting state.

Phase diagram and magnetic fluctuations. In Fig. 1, we show the computed superconducting phase diagram as a function of chemical potential $\mu \leq 0$ and second-neighbor hopping $t' \leq 0$. We also show the different topologies of the two Fermi surfaces, defined as the zeros of $E_{\mathbf{k}}^{-}$ (blue) and $E_{\mathbf{k}}^{+}$ (red), as well as the lines along which the van Hove singularities of the two quasiparticle bands reach the Fermi level. We note that the density of states and position in k space of the two van Hove singularities are markedly different: VHS1 (left line) has a larger density of states than VHS2 (right line) and is also located further away from the $(\pi, 0)$ point, see Supplementary Information SIV. A large portion of the phase diagram displays a leading superconducting state living in the B_1 representation of the combined spin-lattice symmetry group of Hamiltonian (1) (see Method Section and Supplementary Information SIII for more details). The

resulting gap function can be expressed as

$$\Delta_{\mathbf{k}}^{B_1} = \alpha_s (\cos k_x - \cos k_y) t^0 + \alpha_t (\sin k_y t^1 + \sin k_x t^2) + \text{higher harmonics}, \quad (6)$$

where $t^\mu = i\tau^\mu \tau^2$ (τ^μ , $\mu = 0, \dots, 3$ are the Pauli matrices), and α_s and α_t are free parameters. Note that the singlet component of the gap (the one proportional to t^0) is the $d_{x^2-y^2}$ -wave SC order parameter one would obtain in the Hubbard model without introducing the spin-orbit coupling. At larger absolute values of the chemical potential, we obtain a phase belonging to the A_1 representation of the discrete symmetry group of the Hamiltonian. The SC gap in this state is a superposition of an extended s -wave in the singlet component and a helical p -wave in the triplet:

$$\Delta_{\mathbf{k}}^{A_1} = \alpha_s (\cos k_x + \cos k_y) t^0 + \alpha_t (-\sin k_y t^1 + \sin k_x t^2) + \text{higher harmonics}. \quad (7)$$

For larger $-\mu$ and small $-t'$, we also find a B_2 phase, characterized, however, by rather small values of the leading eigenvalue, resulting in low transition temperatures. The gap function in this phase is given by:

$$\Delta_{\mathbf{k}}^{B_2} = \alpha_s \sin k_x \sin k_y t^0 + \alpha_t (\sin k_x t^1 - \sin k_y t^2) + \text{higher harmonics}. \quad (8)$$

We remark that the transition lines in Fig. 1 only mark the crossing between two eigenvalues, and a superconducting state resulting from the superposition of two neighboring phases can be expected near the phase boundaries. At the bottom left of the phase diagram in Fig. 1, that is, for small $-\mu$ and $-t'$, we labeled as iAF (incommensurate antiferromagnetism) the region where the fRG flow finds magnetism as the leading instability.

In the upper left panel of Fig. 2, we plot the parameter η ,

$$\eta = \frac{\sum_{\mu=1}^3 \int_{\mathbf{k}} \text{Tr} \left[\frac{1}{2} \Delta_{\mathbf{k}}(t^{\mu})^{\dagger} \right]^2}{\sum_{\mu=0}^3 \int_{\mathbf{k}} \text{Tr} \left[\frac{1}{2} \Delta_{\mathbf{k}}(t^{\mu})^{\dagger} \right]^2}, \quad (9)$$

quantifying the strength of spin-triplet in the leading superconducting state. Values of η that are close to zero imply a singlet-dominated SC state, while $\eta \sim 1$ implies a triplet-dominated state. We note that the B_1 phase is mostly singlet-dominated, reminiscent of the d -wave SC state emerging in the Hubbard model without spin-orbit coupling. Conversely, the A_1 phase is triplet-dominated in a broad region in between the two van-Hove singularities for large values of $-t'$. This property can be understood by analyzing the spin fluctuations in the model, which are responsible for pairing [24, 25]. In the insets of panels (c) and (d) of Fig. 2, we plot the momentum dependence of the transverse and longitudinal static spin susceptibility, probing the spin fluctuations in and out of the plane defined by the lattice, respectively. In the main panels, we show the ratio between the susceptibility evaluated at $\mathbf{q} = \mathbf{0}$ and its maximum in the Brillouin zone, which gives a good indication of the strength of ferromagnetic fluctuations. When this ratio gets close to one, the largest peak of the relative susceptibility is to be found close to $\mathbf{q} = \mathbf{0}$, viceversa, when it is close to zero the peak is far away from $\mathbf{q} = \mathbf{0}$. This is the case of the region where a magnetic instability is found, due to a divergence of the transverse susceptibility for \mathbf{q} near the antiferromagnetic wave-vector (π, π) . The comparison between panels (a), (c) and (d) of Fig. 2 is very instructive. Indeed, we note that spin fluctuations peaked around (π, π) tend to favor a B_1 singlet-dominated pairing, while ferromagnetic fluctuations enhance a triplet-dominated A_1 state.

In panel (b) of Fig. 2, we also report the value of the leading superconducting eigenvalue λ_{SC} , which provides information on the relative size of the superconducting transition temperature. Note that $\lambda_{SC} > 1$ implies that the critical temperature is higher than the temperature at which the calculations have been performed, that is, $T = 10^{-6}t$. The superconducting eigenvalue is maximum along the van Hove lines and close to the magnetically unstable region, where spin fluctuations are stronger in absolute value, and it decays by moving away from it. Along the leftmost van Hove line, it decays mildly, remaining large even down to $t' = -0.5t$, producing robust spin-triplet-dominated superconductivity in this region. Within the fRG+MFT scheme, the transition tempera-

ture T_c can be estimated either as the temperature at which the vertex function diverges or as the lowest temperature at which the mean-field gap equation returns a zero order parameter, corresponding to the point where $\lambda_{SC} = 1$. By construction, both criteria yield the same transition temperature. The behavior of the critical temperature as a function of the chemical potential and second neighbor hopping resembles the one of the superconducting eigenvalue (panel (b) of Fig. 2) and it reaches its maximum values, of the order of $10^{-2}t$, along the van Hove line, next to the antiferromagnetic instability. For large values of $|t'|$, T_c is of the order of $10^{-3}t$ - $10^{-4}t$ in the vicinity of the van Hove singularity, and it decays away from it.

Having understood the origin of different superconducting phases in Fig. 1, we then focus on each of them individually by investigating the characteristic points marked by black crosses in Fig. 1. In particular, we characterize the topological properties of the superconducting phases by looking at the corresponding edge states. We use a hybrid method of fRG+MFT where we obtain the effective interaction strengths in different superconducting channels from fRG. Using these interactions we perform a renormalized mean-field theory in real space, as detailed in the Method Section and Supplementary Information SIII. Furthermore, we scale the interaction strengths by 10 in order to investigate the edge properties.

B_1 pairing state. In Fig. 3, we investigate the properties of the B_1 phase for the parameters marked by cross I ($\mu = -0.5$ and $t' = -0.5$) in Fig. 1. We first plot in Fig. 3(a) the absolute value of the intraband superconducting gap functions Δ_k^{++} (shown for $k_x < 0$) and Δ_k^{--} (shown for $k_x > 0$) with a periodic boundary condition. The interband components are small and hence we do not show them here. Since the leading instability is B_1 with mostly singlet components (see Fig. 2(a)), the order parameter has primarily d -wave symmetry and consequently the gap functions show nodes along the diagonal $k_x = \pm k_y$. This nodal structure suggests that a (11) edge is pair-breaking [52, 53] and will form topological zero-energy states [54–57] protected by time-reversal symmetry and translational symmetry along (11). To investigate the edge properties, we consider an open boundary geometry (see Fig. 3(b)) with one (11) edge. At intermediate temperatures ($1 > T/T_c > 0.17$), we find a flat band of zero-energy states as shown by red dots in Fig. 3(c). The large degeneracy of these zero-energy states make them thermodynamically unstable and prone to symmetry breaking. Thus at lower temperatures, $T/T_c < 0.17$, the (11) edge hosts oscillations in the phase θ of the d -wave superconducting order parameter, see (b). Such oscillations are often referred to as phase crystals breaking both time-reversal symmetry and translational symmetry along the (11) edge [47–49]. In comparison to earlier literature on phase crystals, one remarkable feature of the phase crystals obtained here is that they are robust to the additional presence of a

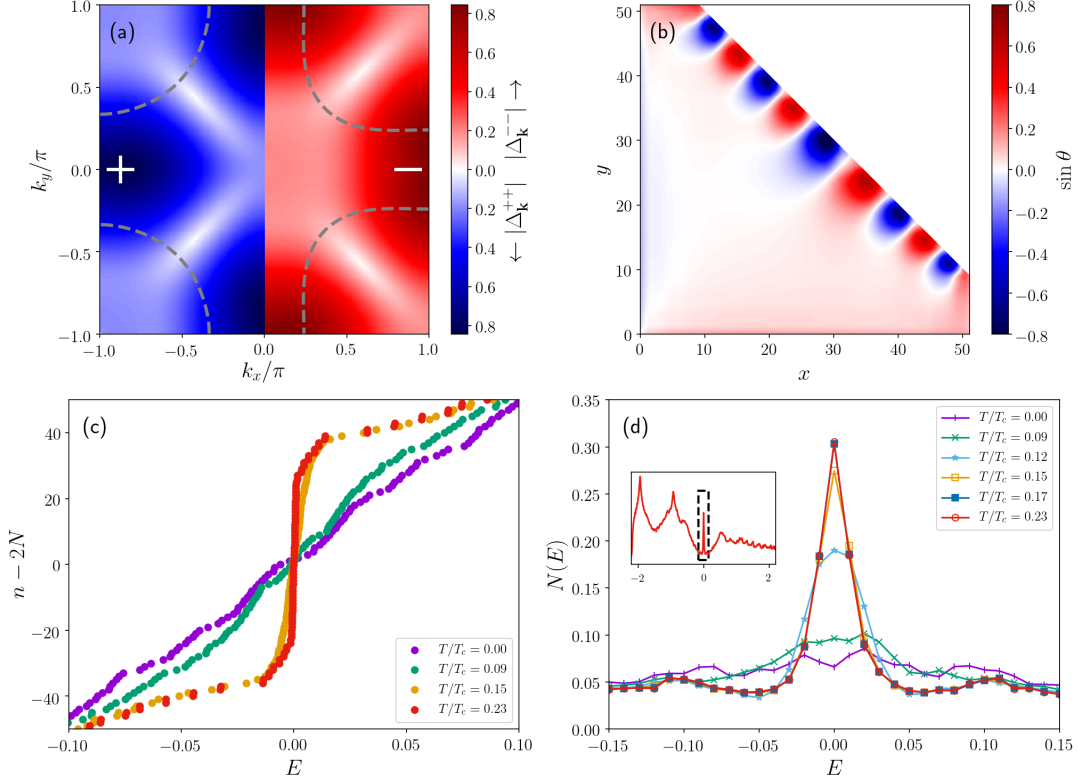


Figure 3. **B₁ pairing state.** (a) Momentum dependence of the B₁ gap function for intraband order parameters at $T = 0$. $k_x > 0$ and $k_x < 0$ shows the contributions from the two different helicity bands. Dashed lines indicate the Fermi surface of the corresponding helicity band. (b) Phase crystal forming at the (11) edge. The sine of the phase θ of the d -wave superconducting order parameter is plotted in real space at $T = 0$ with the bulk value of $\sin \theta$ being subtracted. At the (11) edge there are clear modulations visible in $\sin \theta$. (c) Eigenvalues E around zero energy for different temperature T/T_c . n is the eigen index with twice the total number of sites $2N$ being subtracted. All energies are in units of t . (d) Density of states $N(E)$ around zero energy for different temperatures T/T_c . The inset shows the density of states at $T/T_c = 0.23$ in a wider range.

subdominant A_1 superconducting order parameter originating in the bulk due to the spin-orbit coupling. The formation of phase crystals Doppler shifts the zero-energy states to finite energies, as shown in Fig. 3(c). With lowering temperature, the shift increases. We also calculate the spatially averaged density of states $N(E) = 1/N \sum_{i,n,\sigma} |u_{i\sigma}^n|^2 \delta(E - E_n) + |v_{i\sigma}^n|^2 \delta(E + E_n)$, where N is the total number of lattice sites, and $u_{i\sigma}^n$ and $v_{i\sigma}^n$ are the eigenfunctions with eigenvalues E . To numerically evaluate $N(E)$, we use a Lorentzian with fixed width 0.01 to calculate the delta-function. As shown in Fig. 3(d), $N(E)$ shows a large zero-bias peak for $T/T_c > 0.17$ which does not change with increasing temperature. Due to the formation of the phase crystal at $T/T_c \approx 0.17$, the zero-bias peak gets suppressed for lower temperatures. We do not find a full gap in $N(E)$ even at the lowest temperature, suggesting that there is no formation of extended s -wave phase at the edge.

A₁ pairing state. We now investigate the topological edge states of the A_1 phase for the parameters marked by cross III ($\mu = -1.6$ and $t' = -0.5$) in Fig. 1. In Fig. 4(a), we first show the absolute values of intraband superconducting gap functions obtained with periodic

boundary condition. As seen, the gap functions feature point nodes, but away from the Fermi surface. These nodes are accidental as they can be moved by changing parameters of the model. Due to the lack of nodes on the Fermi surface, we find a full gap in the spectrum (not shown). With this A_1 pairing, the system is a time-reversal symmetric superconductor and belongs to the DIII class, characterized by a \mathbb{Z}_2 invariant in two dimension [3]. In our case, there is one pocket around the M point with negative pairing and the system is topologically nontrivial according to $N_{2D} = \Pi_s [\text{sgn}(\Delta_s)]^{m_s}$, where m_s is the number of time-reversal invariant points enclosed by the s th Fermi surface [58]. To study the topological edge states, we then consider a nanoribbon geometry with open boundary conditions along x and periodic boundary conditions along y . Here, we show the results for the nanoribbon geometry with no self-consistency on the order parameters, in order to reach a large system size. We obtain the self-consistent order parameters with periodic boundary conditions along both x and y , and using this self-consistent solution we employ the nanoribbon geometry with no further self-consistency. We have however verified for a smaller sys-

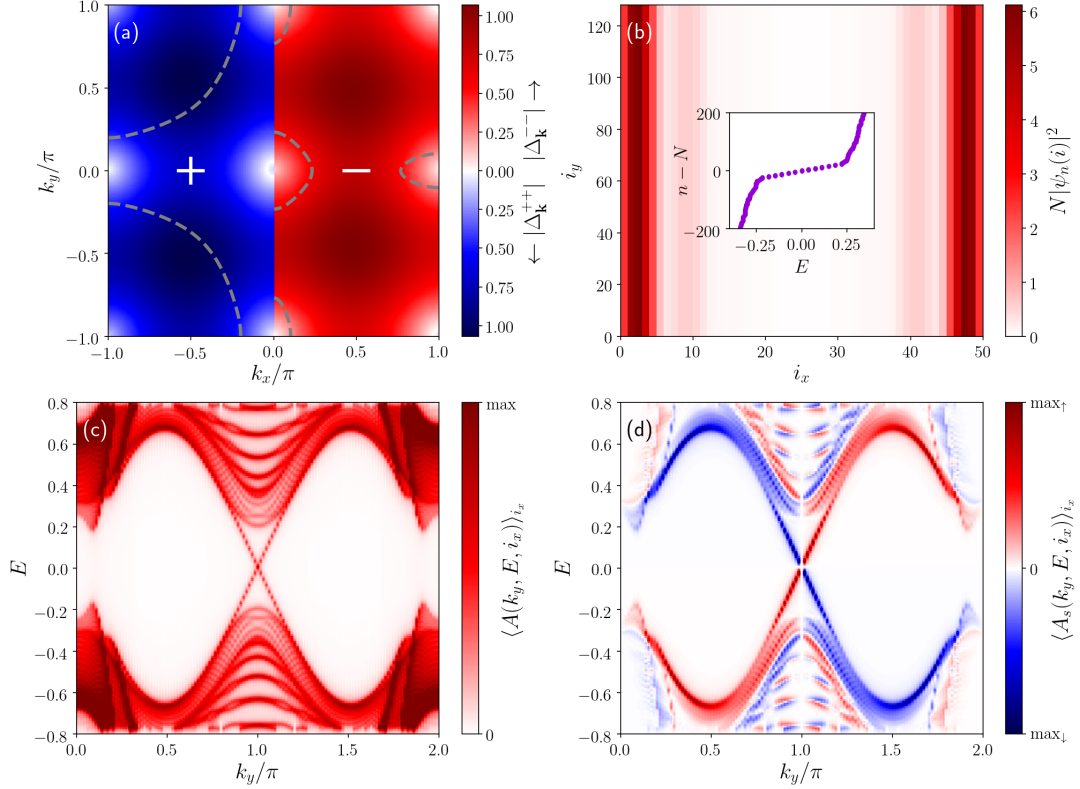


Figure 4. **A_1 pairing state.** (a) Momentum dependence of the A_1 gap function for intraband order parameters. $k_x > 0$ and $k_x < 0$ shows the contributions from the two different helicity bands. Dashed lines indicate the Fermi surface of the corresponding helicity band. (b) Position dependence of the wave-function amplitude of the lowest positive eigenstate near zero-energy for a nanoribbon with open boundary conditions along x and periodic boundary conditions along y . The inset shows the eigenvalues. (c) Momentum resolved density of states averaged over x , $\langle A(k_y, E, i_x) \rangle_{i_x}$, showing linearly dispersing edge states. (d) Momentum resolved spin density of states averaged over a width near the left (10) edge of the nanoribbon, $\langle A_s(k_y, E, i_x) \rangle_{i_x}$, showing the helical nature of the edge states. All the plots are for $T = 0$. All energies are in units of t . The maximum values of the colorbars in (c) and (d) are cut for better visibility.

tem size that all the edge features are insensitive to self-consistency. In the inset of Fig. 4(b), we show the eigenvalues for the nanoribbon geometry. As seen, there are in-gap edge states formed for $|E| < 0.2$. We also show the wavefunction $|\psi_n(i)|^2 = \sum_{\sigma} (|u_{i\sigma}^n|^2 + |v_{i\sigma}^n|^2)$ for the lowest positive eigenstate with $E \approx 0$ in the main panel of Fig. 4(b). The wavefunction is localized to the open (10) edges with oscillating weights going away from the edge. The localization length is less than the half of the length along x -direction, thus prohibiting any interference of the two edges. Using translational symmetry along the y -direction, we look at the edge spectrum by calculating the momentum resolved density of states $A(k_y, E, i_x) = \sum_{n,\sigma} |u_{i_x, k_y, \sigma}^n|^2 \delta(E - E_n)$ and spin density of states $A_s(k_y, E, i_x) = \sum_{n,\sigma} \text{sgn}(\sigma) |u_{i_x, k_y, \sigma}^n|^2 \delta(E - E_n)$, where $u_{i_x, k_y, \sigma}^n$ is the Fourier transform of $u_{i, \sigma}^n$ along the y -direction with i_x being the x -coordinate of the lattice site i and E_n is the eigenenergy of the state n . In Fig. 4(c), we show $A(k_y, E, i_x)$ averaged over all i_x . We find a linearly dispersing Dirac edge spectrum inside the gap $E = 0.2$ at $k_y = \pi$. To identify the spin character of

the edge states, we show in Fig. 4(d) $A_s(k_y, E, i_x)$ averaged over $i_x = 0, 10$ from the left (10) edge. The spectrum clearly shows a helical nature of the edge states with positive values for positive velocities and negative for negative velocities. The corresponding $A_s(k_y, E, i_x)$ averaged over $i_x = 0, 10$ from the right (10) edge shows an opposite behavior, not shown. The helical Majorana edge modes clearly demonstrate the nontrivial topology of the A_1 superconducting phase.

$A_1 + iB_1$ pairing state. The transition from the B_1 superconducting state to the A_1 state with increasing $|\mu|$ in Fig. 1 gives the possibility of a coexisting phase where both order parameters are comparable. To explore this possibility, we fix the parameters to the values marked by cross II ($\mu = -1.2$ and $t' = -0.5$) in Fig. 1, which is near the phase boundary. Interestingly, we find a time-reversal symmetry breaking $A_1 + iB_1$ superconducting phase as the lowest energy state. The corresponding gap functions are shown in Fig. 5(a). Again, the nodes do not lie on the Fermi surface making the state fully gapped with an energy gap of $E = 0.25$. To verify that the relative phase of $\pi/2$ between the A_1 and

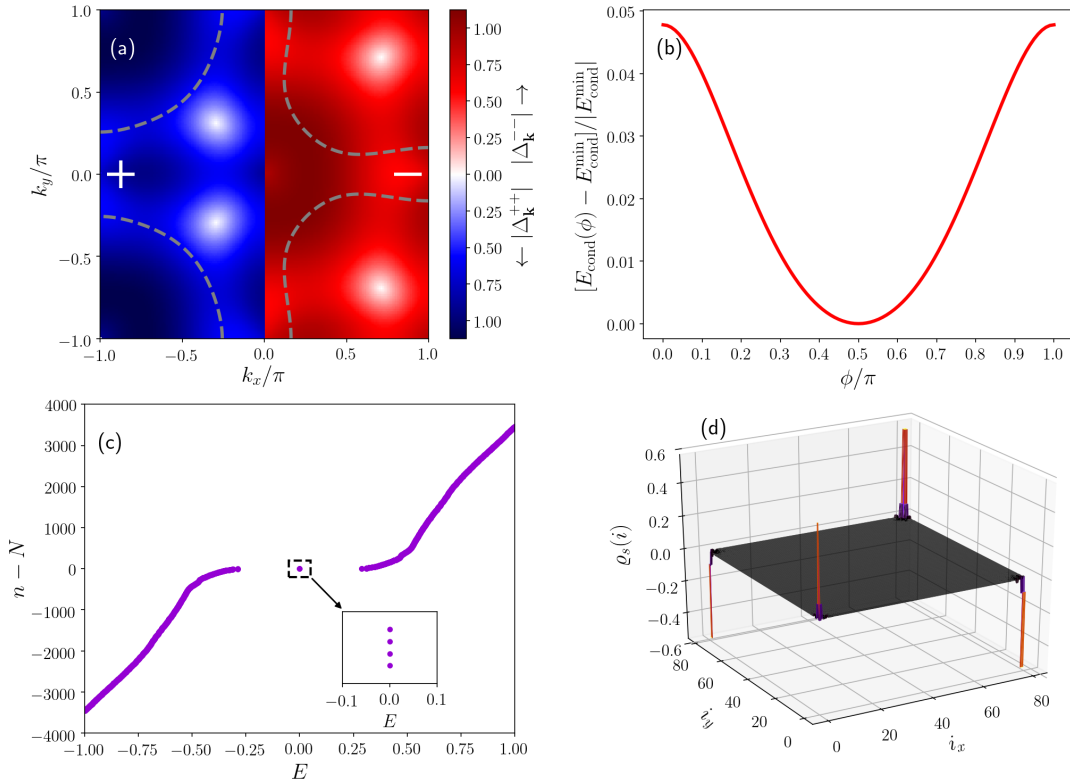


Figure 5. **$A_1 + iB_1$ pairing state.** (a) Momentum dependence of the $A_1 + iB_1$ gap function for intraband order parameters. $k_x > 0$ and $k_x < 0$ shows the contributions from the two different helicity bands. Dashed lines indicate the Fermi surface of the corresponding helicity band. (b) Condensation energy as a function of the relative phase ϕ between A_1 and B_1 order parameters, showing $\pi/2$ as the lowest in energy. (c) Eigenvalues with open boundary conditions along both x and y , showing four Majorana states. Inset shows a zoomed view of the four Majorana states. (d) Spin projected wave function of the four Majorana states as a function of position. All the plots are for $T = 0$ and the energies are in units of t .

the B_1 order parameters is indeed the global minimum, we compare the condensation energies of the superconducting states with different relative phase ϕ . As shown in Fig. 5(b), $\phi = \pm\pi/2$ gives the largest condensation energy and consequently $A_1 \pm iB_1$ is lowest in energy. Due to the imaginary B_1 pairing component, time-reversal symmetry and four-fold rotational symmetry C_4 are broken in this pairing state but their combination is preserved, leading to a gap opening in the helical Majorana edge states. However, owing to the sign change of the B_1 pairing under C_4 , the mass terms for adjacent edges [(10) and (01) edges] have opposite sign. Therefore, when these two edges meet at the corners, the mass term vanishes and Majorana corner modes are generated, realizing a second-order topological superconductor [38] (a detailed analysis is given in the Supplementary Information SV). To demonstrate this nontrivial topology, we study the corner states in a geometry with open boundary conditions along both x - and y -directions. Similar to the A_1 phase, we only consider non self-consistent eigenstates with open boundaries taking the fully self-consistent bulk solutions. Remarkably, we find four Majorana zero-energy states located in the superconducting gap, as shown in Fig. 5(c). The wavefunctions corresponding to

these Majorana states are localized at the four corners, not shown. Spin characteristics of these Majorana states can be visualized by looking at the spin projected wavefunctions $\rho_s(i) = \sum_{\sigma n'} \text{sgn}(\sigma) (|u_{i\sigma}^{n'}|^2 + |v_{i\sigma}^{n'}|^2)$ where n' are the four zero-energy states. In Fig. 5(d), we see that $\rho_s(i)$ is localized at the four corners with alternating signs for alternating corners. We have also verified the presence of Majorana corner states in a self-consistent calculation with edges for smaller system sizes. Therefore, the Majorana corner states in our numerical calculations confirm that the $A_1 + iB_1$ state is a higher-order topological superconductor.

Discussion

We have shown that the combined effects of van Hove singularities, Rashba spin-orbit coupling (SOC), and repulsive Hubbard interactions give rise to a cascade of topological superconducting states, including a nodal B_1 state (d -wave like) with flat-band Majorana edge modes, a fully gapped A_1 state (p -wave like) with helical Majorana edge modes, and a time-reversal breaking $A_1 + iB_1$ state with Majorana corner modes. While the first two pairing states have first order topology, characterized

by a winding number and a Pfaffian Z_2 invariant, respectively, the third one exhibits higher-order topology. Since Rashba SOC breaks inversion symmetry, all three phases consist of a mixture of spin-singlet and spin-triplet Cooper pairs, whose relative ratio, however, is vastly different: The B_1 and A_1 states have dominant singlet and triplet pairing, respectively, whereas the $A_1 + iB_1$ is composed of an almost equal amount of singlet and triplet Cooper pairs. The pairing glue for these superconductors is provided by ferro- and antiferromagnetic spin fluctuations, which are strongly enhanced near the van Hove fillings. Interestingly, the Rashba SOC splits the van Hove singularity at the X point of the square lattice into two *different types*, namely, VHS1 which shifts along the $X - \Gamma$ direction and VHS2 which is moved in the $X - M$ direction, see Supplementary Information SIV. For fillings near VHS2 the spin fluctuations are largely ferromagnetic leading to A_1 superconductivity with predominantly triplet pairing, whereas for fillings close to VHS1 incommensurate spin fluctuations give rise to $A_1 + iB_1$ superconductivity. Remarkably, the divergence at VHS1 is considerably stronger than the one at VHS2, implying that the higher-order topological superconductor has the largest T_c . As a consequence, correlated Rashba materials whose Fermi level can be tuned to VHS1 are good candidates for intrinsic higher-order topological superconductors.

It is remarkable that we find the above three topological superconductors in a single phase diagram with only onsite Hubbard interactions. We emphasize that they emerge robustly in the Rashba-Hubbard model, independent of the size of the Rashba SOC and survive the inclusion of further neighbor hoppings. Although we have presented here only results for the square lattice, we expect these topological superconductors to arise also in other 2D lattices, e.g., the triangular or the honeycomb lattice, although with modified irreps, due to the different spin-lattice symmetry groups. For example, in the triangular lattice the B_1 phase would become an $E_2 + iE_2'$ pairing state (chiral d -wave like). Finally, we remark that due to their topological nature these superconducting phases survive moderately strong disorder [59–64], which we exemplified in the Supplementary Information SVI for non-magnetic onsite disorder with box distributions.

Our results provide a guide to understand and design topological superconductivity in heavy-atom superlattices and van der Waals materials. The high variability of these materials may allow to tune the Fermi level to the van Hove fillings, such that an intrinsic topological superconductor with large T_c can be realized. For example, in LAO/STO it is possible to tune the carrier density, and therefore the Fermi surface, by electric gating [20]. This may open up a route to use intrinsic topological superconductors for the design of quantum information devices. Moreover, the $A_1 + iB_1$ superconductor may show interesting diode [65, 66] and piezoelectric effects [67], since it breaks both inversion and time-reversal symmetry.

Methods

fRG+MFT approach. To determine the leading instabilities of the Rashba-Hubbard model, we employ a truncated unity renormalization procedure using the temperature flow. For simplicity we truncate the effective action at the two-particle level and ignore the flow of the self-energy. The particle-particle and particle-hole channels are expanded in a complete basis of form factors (truncated unity approach). To continue the flow below the stopping temperature and to detect the superconducting instabilities, the functional renormalization group is combined with a momentum-space mean field theory. In the presence of disorder or edges the renormalized mean-field equations are solved in real space. For more details see Supplementary Information SI and SIII.

Symmetry classification of superconducting gap.

The spin-lattice symmetries of the square lattice Rashba-Hubbard model form a group with eight elements that is equivalent to the point group C_{4v} . Its irreducible representations consist of four one-dimensional irreps (A_1 , A_2 , B_1 , B_2) and one two-dimensional irrep (E). The symmetries of the superconducting gaps can therefore be classified according to these irreps, see SII for more details.

Acknowledgements. We are thankful to A. Greco and M. Hirschmann for enlightening discussions. D.C. and A.P.S. thank the Max-Planck-Institute FKF Stuttgart and the YITP Kyoto, respectively, for hospitality during the course of this project.

Data availability. The numerical data of the plots within this paper are available from the authors upon reasonable request.

-
- [1] Beenakker, C. Search for majorana fermions in superconductors. *Annual Review of Condensed Matter Physics* **4**, 113–136 (2013). URL <https://doi.org/10.1146/annurev-conmatphys-030212-184337>.
 - [2] Schnyder, A. P. & Brydon, P. M. R. Topological surface states in nodal superconductors. *Journal of Physics: Condensed Matter* **27**, 243201 (2015). URL <https://dx.doi.org/10.1088/0953-8984/27/24/243201>.
 - [3] Chiu, C.-K., Teo, J. C. Y., Schnyder, A. P. & Ryu, S. Classification of topological quantum matter with symmetries. *Rev. Mod. Phys.* **88**, 035005 (2016). URL <https://link.aps.org/doi/10.1103/RevModPhys.88.035005>.
 - [4] Sato, M. & Ando, Y. Topological superconductors: a review. *Reports on Progress in Physics* **80**, 076501 (2017). URL <https://dx.doi.org/10.1088/1361-6633/aa6ac7>.
 - [5] Sharma, M. M., Sharma, P., Karn, N. K. & Awana, V. P. S. Comprehensive review on topological superconducting materials and interfaces. *Superconductor Science and Technology* **35**, 083003 (2022). URL <https://doi.org/10.1088/1361-6633/ab6ac7>.

- [//dx.doi.org/10.1088/1361-6668/ac6987](https://doi.org/10.1088/1361-6668/ac6987).
- [6] von Rohr, F. O. Chemical principles of intrinsic topological superconductors (2023). 2304.00090.
 - [7] Flensberg, K., von Oppen, F. & Stern, A. Engineered platforms for topological superconductivity and majorana zero modes. *Nature Reviews Materials* **6**, 944–958 (2021). URL <https://doi.org/10.1038/s41578-021-00336-6>.
 - [8] Hao, N. & Hu, J. Topological quantum states of matter in iron-based superconductors: from concept to material realization. *National Science Review* **6**, 213–226 (2018). URL <https://doi.org/10.1093/nsr/nwy142>.
 - [9] Wu, X., Zhang, R.-X., Xu, G., Hu, J. & Liu, C.-X. In the pursuit of majorana modes in iron-based high- T_c superconductors. *Memorial Volume for Shoucheng Zhang* 35–60 (2021). URL https://www.worldscientific.com/doi/abs/10.1142/9789811231711_0005.
 - [10] Yin, J.-X. *et al.* Observation of a robust zero-energy bound state in iron-based superconductor Fe(Te,Se). *Nature Physics* **11**, 543–546 (2015). URL <https://doi.org/10.1038/nphys3371>.
 - [11] Wang, D. *et al.* Evidence for majorana bound states in an iron-based superconductor. *Science* **362**, 333–335 (2018). URL <https://www.science.org/doi/abs/10.1126/science.aao1797>.
 - [12] Shimozawa, M., Goh, S. K., Shibauchi, T. & Matsuda, Y. From kondo lattices to kondo superlattices. *Reports on Progress in Physics* **79**, 074503 (2016). URL <https://dx.doi.org/10.1088/0034-4885/79/7/074503>.
 - [13] Novoselov, K. S., Mishchenko, A., Carvalho, A. & Neto, A. H. C. 2d materials and van der Waals heterostructures. *Science* **353**, aac9439 (2016). URL <https://www.science.org/doi/abs/10.1126/science.aac9439>.
 - [14] Liu, Y. *et al.* Van der Waals heterostructures and devices. *Nature Reviews Materials* **1**, 16042 (2016). URL <https://doi.org/10.1038/natrevmats.2016.42>.
 - [15] Bian, R. *et al.* Recent progress in the synthesis of novel two-dimensional van der Waals materials. *National Science Review* **9** (2021). URL <https://doi.org/10.1093/nsr/nwab164>. Nwab164.
 - [16] Jang, B. G., Lee, C., Zhu, J.-X. & Shim, J. H. Exploring two-dimensional van der Waals heavy-fermion material: Data mining theoretical approach. *npj 2D Materials and Applications* **6**, 80 (2022). URL <https://doi.org/10.1038/s41699-022-00357-x>.
 - [17] Hegger, H. *et al.* Pressure-induced superconductivity in quasi-2d CeRhIn₅. *Phys. Rev. Lett.* **84**, 4986–4989 (2000). URL <https://link.aps.org/doi/10.1103/PhysRevLett.84.4986>.
 - [18] Posey, V. & *et al.* Existence of heavy fermion behavior in a van der Waals layered material (2023). URL <https://meetings.aps.org/Meeting/MAR23/Session/G29.5>. APS March Meeting 2023.
 - [19] Reyren, N. *et al.* Superconducting interfaces between insulating oxides. *Science* **317**, 1196–1199 (2007). URL <https://www.science.org/doi/abs/10.1126/science.1146006>.
 - [20] Caviglia, A. D. *et al.* Electric field control of the LaAlO₃/SrTiO₃ interface ground state. *Nature* **456**, 624–627 (2008). URL <https://doi.org/10.1038/nature07576>.
 - [21] Liu, C. *et al.* Two-dimensional superconductivity and anisotropic transport at KTaO₃ (111) interfaces. *Science* **371**, 716–721 (2021). URL <https://www.science.org/doi/abs/10.1126/science.aba5511>.
 - [22] Mizukami, Y. *et al.* Extremely strong-coupling superconductivity in artificial two-dimensional kondo lattices. *Nature Physics* **7**, 849–853 (2011). URL <https://doi.org/10.1038/nphys2112>.
 - [23] Shimozawa, M. *et al.* Controllable Rashba spin-orbit interaction in artificially engineered superlattices involving the heavy-fermion superconductor CeCoIn₅. *Phys. Rev. Lett.* **112**, 156404 (2014). URL <https://link.aps.org/doi/10.1103/PhysRevLett.112.156404>.
 - [24] Greco, A. & Schnyder, A. P. Mechanism for Unconventional Superconductivity in the Hole-Doped Rashba-Hubbard Model. *Phys. Rev. Lett.* **120**, 177002 (2018). URL <https://link.aps.org/doi/10.1103/PhysRevLett.120.177002>.
 - [25] Greco, A., Bejas, M. & Schnyder, A. P. Ferromagnetic fluctuations in the Rashba-Hubbard model. *Phys. Rev. B* **101**, 174420 (2020). URL <https://link.aps.org/doi/10.1103/PhysRevB.101.174420>.
 - [26] Ghadimi, R., Kargarian, M. & Jafari, S. A. Competing superconducting phases in the interacting two-dimensional electron gas with strong Rashba spin-orbit coupling. *Phys. Rev. B* **99**, 115122 (2019). URL <https://link.aps.org/doi/10.1103/PhysRevB.99.115122>.
 - [27] Wolf, S. & Rachel, S. Spin-orbit coupled superconductivity: Rashba-Hubbard model on the square lattice. *Phys. Rev. B* **102**, 174512 (2020). URL <https://link.aps.org/doi/10.1103/PhysRevB.102.174512>.
 - [28] Nogaki, K. & Yanase, Y. Strongly parity-mixed superconductivity in the Rashba-Hubbard model. *Phys. Rev. B* **102**, 165114 (2020). URL <https://link.aps.org/doi/10.1103/PhysRevB.102.165114>.
 - [29] Biderang, M., Zare, M.-H. & Sinker, J. Proximity-driven ferromagnetism and superconductivity in the triangular Rashba-Hubbard model. *Phys. Rev. B* **105**, 064504 (2022). URL <https://link.aps.org/doi/10.1103/PhysRevB.105.064504>.
 - [30] Kawano, M. & Hotta, C. Phase diagram of the square-lattice Hubbard model with Rashba-type anti-symmetric spin-orbit coupling. *Phys. Rev. B* **107**, 045123 (2023). URL <https://link.aps.org/doi/10.1103/PhysRevB.107.045123>.
 - [31] Beyer, J. *et al.* Rashba spin-orbit coupling in the square-lattice Hubbard model: A truncated-unity functional renormalization group study. *Phys. Rev. B* **107**, 125115 (2023). URL <https://link.aps.org/doi/10.1103/PhysRevB.107.125115>.
 - [32] Kopietz, P., Bartosch, L. & Schütz, F. *Introduction to the Functional Renormalization Group* (Springer Berlin Heidelberg, 2010). URL <https://doi.org/10.1007/978-3-642-05094-7>.
 - [33] Metzner, W., Salmhofer, M., Honerkamp, C., Meden, V. & Schönhammer, K. Functional renormalization group approach to correlated fermion systems. *Rev. Mod. Phys.* **84**, 299–352 (2012). URL <https://link.aps.org/doi/10.1103/RevModPhys.84.299>.
 - [34] Wang, J., Eberlein, A. & Metzner, W. Competing order in correlated electron systems made simple: Consistent fusion of functional renormalization and mean-field theory. *Phys. Rev. B* **89**, 121116(R) (2014). URL <https://link.aps.org/doi/10.1103/PhysRevB.89.121116>.
 - [35] Yamase, H., Eberlein, A. & Metzner, W. Coexistence of Incommensurate Magnetism and Superconductivity in the Two-Dimensional Hubbard Model. *Phys. Rev. Lett.*

- 116, 096402 (2016). URL <https://link.aps.org/doi/10.1103/PhysRevLett.116.096402>.
- [36] Vilardi, D., Bonetti, P. M. & Metzner, W. Dynamical functional renormalization group computation of order parameters and critical temperatures in the two-dimensional Hubbard model. *Phys. Rev. B* **102**, 245128 (2020). URL <https://link.aps.org/doi/10.1103/PhysRevB.102.245128>.
- [37] Bonetti, P. M. Accessing the ordered phase of correlated Fermi systems: Vertex bosonization and mean-field theory within the functional renormalization group. *Phys. Rev. B* **102**, 235160 (2020). URL <https://link.aps.org/doi/10.1103/PhysRevB.102.235160>.
- [38] Wang, Y., Lin, M. & Hughes, T. L. Weak-pairing higher order topological superconductors. *Phys. Rev. B* **98**, 165144 (2018). URL <https://link.aps.org/doi/10.1103/PhysRevB.98.165144>.
- [39] Yan, Z., Song, F. & Wang, Z. Majorana corner modes in a high-temperature platform. *Phys. Rev. Lett.* **121**, 096803 (2018). URL <https://link.aps.org/doi/10.1103/PhysRevLett.121.096803>.
- [40] Wang, Q., Liu, C.-C., Lu, Y.-M. & Zhang, F. High-temperature majorana corner states. *Phys. Rev. Lett.* **121**, 186801 (2018). URL <https://link.aps.org/doi/10.1103/PhysRevLett.121.186801>.
- [41] Wu, X., Liu, X., Thomale, R. & Liu, C.-X. High-Tc superconductor Fe(Se,Te) monolayer: an intrinsic, scalable and electrically tunable Majorana platform. *National Science Review* **9** (2021). URL <https://doi.org/10.1093/nsr/nwab087>. Nwab087.
- [42] Hsu, Y.-T., Cole, W. S., Zhang, R.-X. & Sau, J. D. Inversion-protected higher-order topological superconductivity in monolayer WTe_2 . *Phys. Rev. Lett.* **125**, 097001 (2020). URL <https://link.aps.org/doi/10.1103/PhysRevLett.125.097001>.
- [43] Kheirikhah, M., Yan, Z., Nagai, Y. & Marsiglio, F. First- and second-order topological superconductivity and temperature-driven topological phase transitions in the extended hubbard model with spin-orbit coupling. *Phys. Rev. Lett.* **125**, 017001 (2020). URL <https://link.aps.org/doi/10.1103/PhysRevLett.125.017001>.
- [44] Wu, X. *et al.* Boundary-obstructed topological high- t_c superconductivity in iron pnictides. *Phys. Rev. X* **10**, 041014 (2020). URL <https://link.aps.org/doi/10.1103/PhysRevX.10.041014>.
- [45] Ikegaya, S., Rui, W. B., Manske, D. & Schnyder, A. P. Tunable majorana corner modes in noncentrosymmetric superconductors: Tunneling spectroscopy and edge imperfections. *Phys. Rev. Res.* **3**, 023007 (2021). URL <https://link.aps.org/doi/10.1103/PhysRevResearch.3.023007>.
- [46] Li, T., Geier, M., Ingham, J. & Scammell, H. D. Higher-order topological superconductivity from repulsive interactions in kagome and honeycomb systems. *2D Materials* **9**, 015031 (2021). URL <https://dx.doi.org/10.1088/2053-1583/ac4060>.
- [47] Håkansson, M., Löfwander, T. & Fogelström, M. Spontaneously broken time-reversal symmetry in high-temperature superconductors. *Nat. Phys.* **11**, 755–760 (2015). URL <https://doi.org/10.1038/nphys3383>.
- [48] Holmval, P., Fogelström, M., Löfwander, T. & Vorontsov, A. B. Phase crystals. *Phys. Rev. Research* **2**, 013104 (2020). URL <https://link.aps.org/doi/10.1103/PhysRevResearch.2.013104>.
- [49] Chakraborty, D., Löfwander, T., Fogelström, M. & Black-Schaffer, A. M. Disorder-robust phase crystal in high-temperature superconductors stabilized by strong correlations. *npj Quantum Materials* **7**, 44 (2022). URL <https://doi.org/10.1038/s41535-022-00450-w>.
- [50] Nayak, C., Simon, S. H., Stern, A., Freedman, M. & Das Sarma, S. Non-abelian anyons and topological quantum computation. *Rev. Mod. Phys.* **80**, 1083–1159 (2008). URL <https://link.aps.org/doi/10.1103/RevModPhys.80.1083>.
- [51] Zhang, S.-B. *et al.* Topological and holonomic quantum computation based on second-order topological superconductors. *Phys. Rev. Res.* **2**, 043025 (2020). URL <https://link.aps.org/doi/10.1103/PhysRevResearch.2.043025>.
- [52] Kashiwaya, S. & Tanaka, Y. Tunnelling effects on surface bound states in unconventional superconductors. *Rep. Prog. Phys.* **63**, 1641–1724 (2000). URL <https://doi.org/10.1088/2F0034-4885/2F63/2F10/2F202>.
- [53] Löfwander, T., Shumeiko, V. S. & Wendin, G. Andreev bound states in high-tcsuperconducting junctions. *Supercond. Sci. Technol.* **14**, R53–R77 (2001). URL <https://doi.org/10.1088/2F0953-2048/2F14/2F5/2F201>.
- [54] Ryu, S. & Hatsugai, Y. Topological origin of zero-energy edge states in particle-hole symmetric systems. *Phys. Rev. Lett.* **89**, 077002 (2002). URL <https://link.aps.org/doi/10.1103/PhysRevLett.89.077002>.
- [55] Sato, M., Tanaka, Y., Yada, K. & Yokoyama, T. Topology of andreev bound states with flat dispersion. *Phys. Rev. B* **83**, 224511 (2011). URL <https://link.aps.org/doi/10.1103/PhysRevB.83.224511>.
- [56] Schnyder, A. P. & Brydon, P. M. R. Topological surface states in nodal superconductors. *J. Condens. Matter Phys.* **27**, 243201 (2015). URL <https://doi.org/10.1088/2F0953-8984/2F27/2F24/2F243201>.
- [57] Schnyder, A. P., Timm, C. & Brydon, P. M. R. Edge currents as a signature of flatbands in topological superconductors. *Phys. Rev. Lett.* **111**, 077001 (2013). URL <https://link.aps.org/doi/10.1103/PhysRevLett.111.077001>.
- [58] Qi, X.-L., Hughes, T. L. & Zhang, S.-C. Topological invariants for the fermi surface of a time-reversal-invariant superconductor. *Phys. Rev. B* **81**, 134508 (2010). URL <https://link.aps.org/doi/10.1103/PhysRevB.81.134508>.
- [59] Queiroz, R. & Schnyder, A. P. Stability of flat-band edge states in topological superconductors without inversion center. *Phys. Rev. B* **89**, 054501 (2014). URL <https://link.aps.org/doi/10.1103/PhysRevB.89.054501>.
- [60] Queiroz, R. & Schnyder, A. P. Helical majorana surface states of strongly disordered topological superconductors with time-reversal symmetry. *Phys. Rev. B* **91**, 014202 (2015). URL <https://link.aps.org/doi/10.1103/PhysRevB.91.014202>.
- [61] Lu, Y., Virtanen, P. & Heikkilä, T. T. Effect of disorder on majorana localization in topological superconductors: A quasiclassical approach. *Phys. Rev. B* **102**, 224510 (2020). URL <https://link.aps.org/doi/10.1103/PhysRevB.102.224510>.
- [62] Garg, A., Randeria, M. & Trivedi, N. Strong correlations make high-temperature superconductors robust against disorder. *Nat. Phys.* **4**, 762–765 (2008). URL <https://doi.org/10.1038/nphys1026>.
- [63] Chakraborty, D. & Ghosal, A. Fate of disorder-induced

- inhomogeneities in strongly correlated d-wave superconductors. *New J. Phys.* **16**, 103018 (2014). URL <https://doi.org/10.1088%2F1367-2630%2F16%2F10%2F103018>.
- [64] Ghosal, A., Chakraborty, D. & Kaushal, N. Prospects of anderson's theorem for disordered cuprate superconductors. *Physica B Condens. Matter* **536**, 867 – 876 (2018). URL <http://www.sciencedirect.com/science/article/pii/S0921452617305252>.
- [65] Ando, F. *et al.* Observation of superconducting diode effect. *Nature* **584**, 373–376 (2020). URL <https://doi.org/10.1038/s41586-020-2590-4>.
- [66] Daido, A., Ikeda, Y. & Yanase, Y. Intrinsic superconducting diode effect. *Phys. Rev. Lett.* **128**, 037001 (2022). URL <https://link.aps.org/doi/10.1103/PhysRevLett.128.037001>.
- [67] Chazono, M., Watanabe, H. & Yanase, Y. Superconducting piezoelectric effect. *Phys. Rev. B* **105**, 024509 (2022). URL <https://link.aps.org/doi/10.1103/PhysRevB.105.024509>.
- [68] Honerkamp, C. & Salmhofer, M. Temperature-flow renormalization group and the competition between superconductivity and ferromagnetism. *Phys. Rev. B* **64**, 184516 (2001). URL <https://link.aps.org/doi/10.1103/PhysRevB.64.184516>.
- [69] Wetterich, C. Exact evolution equation for the effective potential. *Phys. Lett. B* **301**, 90 – 94 (1993). URL <http://www.sciencedirect.com/science/article/pii/037026939390726X>.
- [70] Husemann, C. & Salmhofer, M. Efficient parametrization of the vertex function, Ω scheme, and the t, t' Hubbard model at van Hove filling. *Phys. Rev. B* **79**, 195125 (2009). URL <https://link.aps.org/doi/10.1103/PhysRevB.79.195125>.
- [71] Husemann, C., Giering, K.-U. & Salmhofer, M. Frequency-dependent vertex functions of the (t, t') Hubbard model at weak coupling. *Phys. Rev. B* **85**, 075121 (2012). URL <https://link.aps.org/doi/10.1103/PhysRevB.85.075121>.
- [72] Lichtenstein, J. *et al.* High-performance functional Renormalization Group calculations for interacting fermions. *Comput. Phys. Commun.* **213**, 100 – 110 (2017). URL <http://www.sciencedirect.com/science/article/pii/S0010465516303927>.
- [73] Schober, G. A. H., Ehrlich, J., Reckling, T. & Honerkamp, C. Truncated-Unity Functional Renormalization Group for Multiband Systems With Spin-Orbit Coupling. *Front. Phys.* **6** (2018). URL <https://www.frontiersin.org/articles/10.3389/fphy.2018.00032>.
- [74] Platt, C., Hanke, W. & Thomale, R. Functional renormalization group for multi-orbital fermi surface instabilities. *Adv. Phys.* **62**, 453–562 (2013). URL <https://doi.org/10.1080/00018732.2013.862020>.
- [75] Zhu, J. *Bogoliubov-de Gennes Method and Its Applications*. Lecture Notes in Physics (Springer International Publishing, 2016). URL <https://books.google.se/books?id=Tep6DAAAQBAJ>.
- [76] Schnyder, A. P., Brydon, P. M. R. & Timm, C. Types of topological surface states in nodal noncentrosymmetric superconductors. *Phys. Rev. B* **85**, 024522 (2012). URL <https://link.aps.org/doi/10.1103/PhysRevB.85.024522>.

Supplementary Information - van Hove, Rashba, and Hubbard meet to form first-order and higher-order topological superconductors

This Supplementary Information contains six sections. In [SI](#) we discuss the details of the truncated unity renormalization group procedure and explain how it is combined with a momentum-space mean-field theory. In [SII](#) we present the symmetry classification of the superconducting states in terms of the irreps of the spin-lattice group. In [SIII](#) we provide the details of the real space renormalized mean-field theory and show how it is matched to the fRG. In [SIV](#) effective models for the van Hove singularities are derived and analyzed. In [SV](#) the corner modes of the $A_1 + iB_1$ pairing state are discussed. The effects of disorder are studied in [SVI](#).

SI. FRG+MFT METHOD

In this section we provide some details on the fRG+MFT method, employed to determine the leading superconducting symmetry in the Rashba-Hubbard model.

A. Functional renormalization group

In order to determine the system's instabilities and the leading superconducting symmetry, we run a truncated functional renormalization group flow [\[32, 33\]](#). The flow is implemented by a progressive integration of fermionic modes by introducing a flowing cutoff in the bare propagator. Here, we choose the so-called *temperature flow* [\[68\]](#). By rescaling the Grassmann fields according to

$$\eta_{\mathbf{k},\sigma} = T^{\frac{3}{4}} \psi_{\mathbf{k},\sigma}, \quad (\text{S1a})$$

$$\bar{\eta}_{\mathbf{k},\sigma} = T^{\frac{3}{4}} \bar{\psi}_{\mathbf{k},\sigma}, \quad (\text{S1b})$$

where T is the temperature, we obtain the action

$$\mathcal{S}^T[\eta, \bar{\eta}] = \sum_n \int_{\mathbf{k}} \bar{\eta}_{\mathbf{k},n} \left[T^{-\frac{1}{2}} \left(i\nu_n - \hat{\mathcal{H}}_{\mathbf{k}} \right) \right] \eta_{\mathbf{k},n} + U \sum_{n_1, n_2, n_3} \int_{\mathbf{k}_1, \mathbf{k}_2, \mathbf{k}_3} \bar{\eta}_{\mathbf{k}_1, n_1, \uparrow} \bar{\eta}_{\mathbf{k}_2, n_2, \downarrow} \eta_{\mathbf{k}_4, n_4, \downarrow} \eta_{\mathbf{k}_3, n_3, \uparrow},$$

where n labels fermionic Matsubara frequencies $\nu_n = (2n+1)\pi T$ ($n \in \mathbb{Z}$), $\mathbf{k}_4 = \mathbf{k}_1 + \mathbf{k}_2 - \mathbf{k}_3$ and $n_4 = n_1 + n_2 - n_3$, and $\hat{\mathcal{H}}_{\mathbf{k}}$ is defined in Eq. [\(3\)](#). We note that upon rescaling [\(S1\)](#), only the quadratic part of the action remains temperature-dependent, with bare propagator

$$\hat{G}_0^T(\mathbf{k}, \nu_n) = T^{\frac{1}{2}} \left[i\nu_n - \hat{\mathcal{H}}_{\mathbf{k}} \right]^{-1}. \quad (\text{S2})$$

The temperature therefore takes the role of a renormalization group scale and one can derive an exact evolution equation for the effective action functional [\[33, 69\]](#)

$$\frac{d}{dT} \Gamma^T[\eta, \bar{\eta}] = - \sum_n \int_{\mathbf{k}} \bar{\eta}_{\mathbf{k},n} \frac{d}{dT} [\hat{G}_0^T(\mathbf{k}, \nu_n)]^{-1} \eta_{\mathbf{k},n} - \frac{1}{2} \text{Tr} \left[\frac{d}{dT} [\mathbf{G}_0^T]^{-1} \left(\mathbf{\Gamma}^{(2)T}[\eta, \bar{\eta}] \right)^{-1} \right]. \quad (\text{S3})$$

Here, we have defined

$$\mathbf{G}_0^T(\mathbf{k}, \nu_n) = \begin{pmatrix} \hat{G}_0^T(\mathbf{k}, \nu_n) & 0 \\ 0 & -[\hat{G}_0^T(-\mathbf{k}, -\nu_n)]^T \end{pmatrix}, \quad (\text{S4})$$

and

$$\mathbf{\Gamma}^{(2)T}[\eta, \bar{\eta}](x, x') = \begin{pmatrix} \frac{\delta \Gamma^T[\eta, \bar{\eta}]}{\delta \bar{\eta}(x') \delta \eta(x)} & \frac{\delta \Gamma^T[\eta, \bar{\eta}]}{\delta \bar{\eta}(x') \delta \bar{\eta}(x)} \\ \frac{\delta \Gamma^T[\eta, \bar{\eta}]}{\delta \eta(x') \delta \eta(x)} & \frac{\delta \Gamma^T[\eta, \bar{\eta}]}{\delta \eta(x') \delta \bar{\eta}(x)} \end{pmatrix}, \quad (\text{S5})$$

where $x = (\mathbf{k}, n, \sigma)$ and the symbol $[\bullet]^T$ denotes matrix transposition and does not have to be confused with the temperature T . Expanding the effective action functional $\Gamma^T[\eta, \bar{\eta}]$ on both sides of (S3), one can derive an infinite hierarchy of flow equations for the n particle vertices

$$\Gamma^{(2n)T}(x_1, \dots, x_n, x'_1, \dots, x'_n) = \frac{\delta \Gamma^T[\eta, \bar{\eta}]}{\delta \bar{\eta}(x'_1) \dots \delta \bar{\eta}(x'_n) \delta \eta(x_1) \dots \delta \eta(x_n)} \bigg|_{\eta, \bar{\eta}=0}. \quad (\text{S6})$$

Eq. (S3) is completed with an initial condition for the effective action reading as [33]

$$\Gamma^{T \rightarrow +\infty}[\eta, \bar{\eta}] = \mathcal{S}^{T \rightarrow +\infty}[\eta, \bar{\eta}]. \quad (\text{S7})$$

In this work, we *truncate* the effective action at the two-particle level, that is, we set to zero all the three- and more particle correlators. We also ignore the flow of the self-energy, that is, we keep the one-particle vertex fixed to $(\hat{G}_0^T)^{-1}$.

The only vertex function we retain is the two particle vertex

$$V^{\sigma_1 \sigma_2 \sigma_3 \sigma_4, T}(\mathbf{k}_1, \mathbf{k}_2, \mathbf{k}_3, n_1, n_2, n_3) = \Gamma^{(4)T}. \quad (\text{S8})$$

which depends, in principle, on the four spins of the two incoming and two outgoing electrons, and on three momenta and Matsubara frequencies. We introduce a further approximation by neglecting the frequency dependence.

To disentangle the dependence of V^T on the three momenta, we employ a channel decomposition [70, 71]:

$$\begin{aligned} V^{\sigma_1 \sigma_2 \sigma_3 \sigma_4}(\mathbf{k}_1, \mathbf{k}_2, \mathbf{k}_3) = & U(\delta_{\sigma_1 \sigma_3} \delta_{\sigma_2 \sigma_4} - \delta_{\sigma_1 \sigma_4} \delta_{\sigma_2 \sigma_3}) \\ & + P_{\mathbf{k}_1, \mathbf{k}_3}^{\sigma_1 \sigma_2 \sigma_3 \sigma_4}(\mathbf{k}_1 + \mathbf{k}_2) + D_{\mathbf{k}_1, \mathbf{k}_4}^{\sigma_1 \sigma_2 \sigma_3 \sigma_4}(\mathbf{k}_3 - \mathbf{k}_1) - D_{\mathbf{k}_1, \mathbf{k}_3}^{\sigma_1 \sigma_2 \sigma_4 \sigma_3}(\mathbf{k}_2 - \mathbf{k}_3), \end{aligned} \quad (\text{S9})$$

where, to simplify the notation, we have dropped the T -dependence. We refer to P and D as particle-particle and particle-hole channels, respectively. It is clear from Eq. (S7) that at $T \rightarrow +\infty$ one has $V = U$ and therefore $P = D = 0$. The flow equations read as

$$\frac{d}{dT} P_{\mathbf{k}, \mathbf{k}'}^{\sigma_1 \sigma_2 \sigma_3 \sigma_4}(\mathbf{q}) = - \sum_{\substack{s_1, s_2 \\ s_3, s_4}} \int_{\mathbf{p}} V^{\sigma_1 \sigma_2 s_3 s_4}(\mathbf{k}, \mathbf{q} - \mathbf{k}, \mathbf{p}) \dot{\Pi}_{P, \mathbf{p}}^{s_1 s_2 s_3 s_4}(\mathbf{q}) V^{s_1 s_2 \sigma_3 \sigma_4}(\mathbf{p}, \mathbf{q} - \mathbf{p}, \mathbf{k}'), \quad (\text{S10a})$$

$$\frac{d}{dT} D_{\mathbf{k}, \mathbf{k}'}^{\sigma_1 \sigma_2 \sigma_3 \sigma_4}(\mathbf{q}) = 2 \sum_{\substack{s_1, s_2 \\ s_3, s_4}} \int_{\mathbf{p}} V^{\sigma_1 s_2 s_3 s_4}(\mathbf{k}, \mathbf{p} + \mathbf{q}, \mathbf{k} + \mathbf{q}) \dot{\Pi}_{D, \mathbf{p}}^{s_1 s_2 s_3 s_4}(\mathbf{q}) V^{s_1 \sigma_2 \sigma_3 \sigma_4}(\mathbf{p}, \mathbf{k}' + \mathbf{q}, \mathbf{p} + \mathbf{q}), \quad (\text{S10b})$$

with

$$\Pi_{P, \mathbf{p}}^{s_1 s_2 s_3 s_4}(\mathbf{q}) = \sum_n [G_{0, s_3 s_1}^T(\mathbf{p}, \nu_n) G_{0, s_4 s_2}^T(\mathbf{q} - \mathbf{p}, -\nu_n)], \quad (\text{S11a})$$

$$\Pi_{D, \mathbf{p}}^{s_1 s_2 s_3 s_4}(\mathbf{q}) = \sum_n [G_{0, s_4 s_1}^T(\mathbf{p}, \nu_n) G_{0, s_3 s_2}^T(\mathbf{p} + \mathbf{q}, \nu_n)]. \quad (\text{S11b})$$

The symbol $\dot{\Pi}$ is a shorthand for $d\Pi/dT$. To simplify the treatment, we parametrize the spin dependence of P and D as

$$P_{\mathbf{k}, \mathbf{k}'}^{\sigma_1 \sigma_2 \sigma_3 \sigma_4}(\mathbf{q}) = \frac{1}{2} \sum_{\alpha, \beta=0}^3 P_{\mathbf{k}, \mathbf{k}'}^{\alpha \beta}(\mathbf{q}) t_{\sigma_1 \sigma_2}^{\alpha} (t_{\sigma_3 \sigma_4}^{\beta})^{\dagger}, \quad (\text{S12a})$$

$$D_{\mathbf{k}, \mathbf{k}'}^{\sigma_1 \sigma_2 \sigma_3 \sigma_4}(\mathbf{q}) = \frac{1}{2} \sum_{\alpha, \beta=0}^3 D_{\mathbf{k}, \mathbf{k}'}^{\alpha \beta}(\mathbf{q}) \tau_{\sigma_1 \sigma_3}^{\alpha} \tau_{\sigma_2 \sigma_4}^{\beta}, \quad (\text{S12b})$$

where $\tau^{1,2,3}$ are the Pauli matrices, $\tau^0 = \mathbb{1}$, and $t^{\alpha} = i\tau^{\alpha}\tau^2$. To treat the dependence of the channels on \mathbf{k} and \mathbf{k}' , we resort to a *truncated unity* approach [72, 73], that is, we expand them in a complete basis of form factors $\{f_{\mathbf{k}}^{\ell}\}$:

$$X_{\mathbf{k}, \mathbf{k}'}^{\alpha \beta}(\mathbf{q}) = \sum_{\ell, \ell'} X_{\ell \ell'}^{\alpha \beta}(\mathbf{q}) f_{\mathbf{k}}^{\ell} (f_{\mathbf{k}'}^{\ell'})^*, \quad (\text{S13})$$

with $X = P$ or D , and truncate the sum up to a given order. We choose form factors that transform in the irreducible representations of the lattice symmetry group C_{4v} . It is possible to choose $f_{\mathbf{k}}^{\ell}$ in such a way that their real space

representation takes nonzero values only in a given shell of neighbors of a given reference site [74]. It is therefore convenient to truncate the sum (S13) by including all form factors up to a given shell. For our calculations, we truncate the sum to the first shell of neighbors, that is, we only consider the form factors

$$f_{\mathbf{k}}^0 = 1, \quad (\text{S14a})$$

$$f_{\mathbf{k}}^1 = \cos k_x + \cos k_y, \quad (\text{S14b})$$

$$f_{\mathbf{k}}^2 = \cos k_x - \cos k_y, \quad (\text{S14c})$$

$$f_{\mathbf{k}}^3 = \sqrt{2} \sin k_x, \quad (\text{S14d})$$

$$f_{\mathbf{k}}^4 = \sqrt{2} \sin k_y. \quad (\text{S14e})$$

Inserting the identity

$$\delta_{\mathbf{k}, \mathbf{k}'} = \sum_{\ell} f_{\mathbf{k}}^{\ell} (f_{\mathbf{k}'}^{\ell})^* \quad (\text{S15})$$

into (S10), we obtain

$$\frac{d}{dT} X_{\ell\ell'}^{\alpha\beta}(\mathbf{q}) = \frac{1}{2} \zeta_X \sum_{\alpha', \beta'} \sum_{m, m'} X[V]_{\ell m}^{\alpha\beta'}(\mathbf{q}) \tilde{\Pi}_{X, mm'}^{\beta'\alpha'}(\mathbf{q}) X[V]_{m'\ell'}^{\alpha'\beta}(\mathbf{q}), \quad (\text{S16})$$

with $X = P$ or D , $\zeta_P = -1$ and $\zeta_D = +2$. The symbols $P[V]$ and $D[V]$ represent the projection of the full vertex (S9) onto the P and D channels and they read as

$$P[V]_{\ell\ell'}^{\alpha\beta}(\mathbf{q}) = \int_{\mathbf{k}, \mathbf{k}'} \frac{1}{2} \sum_{\substack{\sigma_1, \sigma_2 \\ \sigma_3, \sigma_4}} V^{\sigma_1 \sigma_2 \sigma_3 \sigma_4}(\mathbf{k}, \mathbf{q} - \mathbf{k}, \mathbf{k}') (t_{\sigma_1 \sigma_2}^{\alpha})^{\dagger} t_{\sigma_3 \sigma_4}^{\beta} (f_{\mathbf{k}}^{\ell})^* f_{\mathbf{k}'}^{\ell'}, \quad (\text{S17a})$$

$$D[V]_{\ell\ell'}^{\alpha\beta}(\mathbf{q}) = \int_{\mathbf{k}, \mathbf{k}'} \frac{1}{2} \sum_{\substack{\sigma_1, \sigma_2 \\ \sigma_3, \sigma_4}} V^{\sigma_1 \sigma_2 \sigma_3 \sigma_4}(\mathbf{k}, \mathbf{k}' + \mathbf{q}, \mathbf{k}) \tau_{\sigma_3 \sigma_1}^{\alpha} \tau_{\sigma_4 \sigma_2}^{\beta} (f_{\mathbf{k}}^{\ell})^* f_{\mathbf{k}'}^{\ell'}. \quad (\text{S17b})$$

Similar expressions hold for the bubbles $\tilde{\Pi}_{X, \ell\ell'}^{\beta\alpha}(\mathbf{q})$. For more details on how to perform the vertex projections, see for example Refs. [72, 73].

We run a flow starting from a high-temperature value $T_{\text{ini}} \simeq 10t$ at which P and D can be initialized by a second order perturbation theory result:

$$X_{\ell\ell'}^{\alpha\beta T_{\text{ini}}}(\mathbf{q}) = \frac{1}{2} \zeta_X U^2 \Pi_{X, 00}^{\alpha\beta T_{\text{ini}}}(\mathbf{q}) \delta_{\ell, 0} \delta_{\ell', 0}, \quad (\text{S18})$$

to (approximately) account for the integration from $T = +\infty$ to $T = T_{\text{ini}}$. We stop the flow at a temperature T_c where one of P or D exceeds the value $25t$ or at a temperature $T_{\text{min}} = 10^{-2}t$ where the momentum integration in the projections of the bubbles (S11) onto form factors becomes numerically unstable.

B. Renormalized mean-field theory

To continue the flow below the stopping temperature $T_s \equiv \max(T_c, T_{\text{min}})$, and therefore detect the leading superconducting instabilities, we resort to a combination of mean-field theory with the functional renormalization group [34, 35, 37]. This approximation accounts for continuing the flow in the superconducting regime, that is, by introducing a pairing gap and anomalous vertices, by keeping only particle-particle diagrams. The simplified flow equations can be formally integrated and cast in the form of *renormalized* mean-field equations. In this way, one obtains the gap equation (valid for any $0 \leq T \leq T_s$)

$$\Delta_{\mathbf{k}}^{\sigma\sigma'} = \sum_{s, s'} \int_{\mathbf{k}'} \tilde{V}_{\mathbf{k}\mathbf{k}'}^{\sigma\sigma' ss'} \left[T \sum_n F^{ss'}(\mathbf{k}', \nu_n) \right],$$

where $F^{\sigma\sigma'}(\mathbf{k}, \nu_n)$ are the spin components of the anomalous propagator $\hat{F}(\mathbf{k}, \nu_n)$, defined through

$$\mathbf{G}_{\text{BdG}}(\mathbf{k}, i\nu_n) = \begin{pmatrix} \hat{G}(\mathbf{k}, \nu_n) & \hat{F}(\mathbf{k}, \nu_n) \\ \hat{F}^{\dagger}(\mathbf{k}, \nu_n) & -[\hat{G}(-\mathbf{k}, -\nu_n)]^{\text{T}} \end{pmatrix} = \begin{pmatrix} i\nu_n - \hat{\mathcal{H}}_{\mathbf{k}} & -\hat{\Delta}_{\mathbf{k}} \\ -\hat{\Delta}_{\mathbf{k}}^{\dagger} & i\nu_n + [\hat{\mathcal{H}}_{-\mathbf{k}}]^{\text{T}} \end{pmatrix}^{-1}, \quad (\text{S19})$$

with $\hat{\Delta}_{\mathbf{k}}$ the gap matrix (in spin space). The function $\tilde{V}_{\mathbf{k}\mathbf{k}'}^{\sigma_1\sigma_2\sigma_3\sigma_4}$ is the two-particle-irreducible vertex function in the particle-particle channel at zero center-of-mass momentum. It is determined by inverting a Bethe-Salpeter equation at the stopping temperature T_s :

$$V^{\sigma_1\sigma_2\sigma_3\sigma_4,T_s}(\mathbf{k}, -\mathbf{k}, \mathbf{k}') = \tilde{V}_{\mathbf{k}\mathbf{k}'}^{\sigma_1\sigma_2\sigma_3\sigma_4} + \sum_{\substack{s_1,s_2 \\ s_3,s_4}} \int_{\mathbf{p}} \tilde{V}_{\mathbf{k}\mathbf{p}}^{\sigma_1\sigma_2s_3s_4} \Pi_{P,\mathbf{p}}^{s_1s_2s_3s_4,T_s}(\mathbf{q}=\mathbf{0}) V^{s_1s_2\sigma_3\sigma_4,T_s}(\mathbf{p}, -\mathbf{p}, \mathbf{k}'). \quad (\text{S20})$$

Eq. (S20) can be inverted with an approach similar to the one presented in the previous section: one can parameterize the spin dependence of \tilde{V} , V^{T_s} , and $\Pi_P^{T_s}$ by means of the t^α matrices (see Eq. (S12a)) and expand the \mathbf{k} - and \mathbf{k}' -dependence in form factors and truncate the expansion at a given order. Notice that the order kept in this inversion can be also higher than the one used in the fRG calculation of V^{T_s} . One obtains

$$P[V^{T_s}]_{\ell\ell'}^{\alpha\beta}(\mathbf{q}=\mathbf{0}) = 2\tilde{V}_{\ell\ell'}^{\alpha\beta} + \sum_{\alpha'} \sum_{\beta'} \sum_{m,m'} \tilde{V}_{\ell m}^{\alpha\beta'} \Pi_{P,mm'}^{\beta'\alpha',T_s}(\mathbf{q}=\mathbf{0}) P[V^{T_s}]_{m'\ell'}^{\alpha'\beta}(\mathbf{q}=\mathbf{0}). \quad (\text{S21})$$

Defining a multi-index $\mathbf{i} = (\alpha, \ell)$, \tilde{V} , $P[V^{T_s}]$, and $\Pi_P^{T_s}$ become matrices, and \tilde{V} can be cast as

$$\tilde{V}_{\mathbf{i}\mathbf{i}'} = \left\{ \left[2\mathbf{P}[V^{T_s}](\mathbf{q}=\mathbf{0})^{-1} - \Pi_P^{T_s}(\mathbf{q}=\mathbf{0}) \right]^{-1} \right\}_{\mathbf{i}\mathbf{i}'}. \quad (\text{S22})$$

By expanding also the gap in form factors and t^α matrices, the gap equation takes the form

$$\Delta_\ell^\alpha = \sum_{\beta,\ell'} \tilde{V}_{\ell\ell'}^{\alpha\beta} \mathcal{F}_{\ell'}^\beta, \quad (\text{S23})$$

where we have defined

$$\Delta_{\mathbf{k}}^{\sigma\sigma'} = \sum_{\alpha=0}^3 \sum_{\ell} \Delta_\ell^{\alpha t^\alpha} f_{\mathbf{k}}^\ell, \quad (\text{S24})$$

and

$$\mathcal{F}_{\ell'}^\beta = \frac{1}{2}T \sum_n \int_{\mathbf{k}} \text{Tr} [F(\mathbf{k}, \nu_n)(t^\alpha)^\dagger] (f_{\mathbf{k}}^\ell)^*. \quad (\text{S25})$$

Notice that Eq. (S23) still depends on the temperature via \mathcal{F}_ℓ^α .

Eq. (S23) can be used to determine the gap function at a given temperature $T \geq T_s$ but also to simply determine the leading superconducting state. This can be achieved by *linearizing* it with respect to Δ_ℓ^α . By noticing that

$$\left. \frac{\delta \mathcal{F}_\ell^\alpha}{\delta \Delta_{\ell'}^\beta} \right|_{\Delta_\ell^\alpha=0} = \Pi_{P,\ell\ell'}^{\alpha\beta}(\mathbf{q}=\mathbf{0}), \quad (\text{S26})$$

we obtain

$$\Delta_\ell^\alpha = \sum_{\beta,\gamma} \sum_{\ell',m} \tilde{V}_{\ell\ell'}^{\alpha\beta} \Pi_{P,\ell'm}^{\beta\gamma}(\mathbf{q}=\mathbf{0}) \Delta_m^\gamma. \quad (\text{S27})$$

For temperatures close to the superconducting transition temperature T_{SC} , where the overall magnitude of the gap is small and the linearization carried out above is justifiable, the gap is an eigenvector of the matrix $\tilde{V} \circ \Pi_P(\mathbf{q}=\mathbf{0})$ with eigenvalue 1. T_{SC} can therefore be determined as the temperature at which the largest positive eigenvalue of the matrix $\tilde{V} \circ \Pi_P(\mathbf{q}=\mathbf{0})$ becomes 1. Since in a Fermi liquid some components of $\Pi_P(\mathbf{q}=\mathbf{0})$ diverge like $\log(T^{-1})$ (or $\log^2(T^{-1})$ at a van Hove singularity) as T approaches 0, one will always find a finite value of T_{SC} , or, in other words, Eq. (S23) has always a nontrivial solution at $T=0$. The numerical values of Δ_ℓ^α , however, can be exponentially small, so that their calculation becomes numerically involved. For this reason, we analyze the linearized gap equation, Eq. (S27), at a low temperature, $T_{\text{low}} = 10^{-6}t$, and determine the leading superconducting eigenvalue λ_{SC} , defined as the largest positive eigenvalue of $\tilde{V} \circ \Pi_P(\mathbf{q}=\mathbf{0})$. The symmetry of the corresponding eigenvector determines the symmetry of the leading superconducting instability.

	\mathbf{k}	$\vec{\tau}$	\hat{U}
E	$k_x \rightarrow k_x$ $k_y \rightarrow k_y$	$\tau^1 \rightarrow \tau^1$ $\tau^2 \rightarrow \tau^2$ $\tau^3 \rightarrow \tau^3$	$\mathbb{1}$
C_4^\pm	$k_x \rightarrow \mp k_y$ $k_y \rightarrow \pm k_x$	$\tau^1 \rightarrow \mp \tau^2$ $\tau^2 \rightarrow \pm \tau^1$ $\tau^3 \rightarrow \tau^3$	$e^{\pm i \frac{\pi}{4} \tau^3}$
C_2	$k_x \rightarrow -k_x$ $k_y \rightarrow -k_y$	$\tau^1 \rightarrow -\tau^1$ $\tau^2 \rightarrow -\tau^2$ $\tau^3 \rightarrow \tau^3$	$e^{i \frac{\pi}{2} \tau^3}$
$\Sigma_v^{x(y)}$	$k_x \rightarrow \pm k_x$ $k_y \rightarrow \mp k_y$	$\tau^1 \rightarrow \mp \tau^1$ $\tau^2 \rightarrow \pm \tau^2$ $\tau^3 \rightarrow \tau^3$	$i\tau^3 \mathcal{K} (\mathbb{1} \mathcal{K})$
$\Sigma_d^{1(2)}$	$k_x \rightarrow \pm k_y$ $k_y \rightarrow \pm k_x$	$\tau^1 \rightarrow \mp \tau^2$ $\tau^2 \rightarrow \mp \tau^1$ $\tau^3 \rightarrow \tau^3$	$e^{\pm i \frac{\pi}{4} \tau^3} \mathcal{K}$

Table SI. Discrete spin-lattice transformations that leave the Rashba-Hubbard Hamiltonian invariant. In the first column we show their effect on the lattice momentum \mathbf{k} , in the second one how they transform the Pauli matrices $\vec{\tau}$, and in the third one the operator that implements the spin part of the transformation on the electron operators. We remark that the transformation of the Pauli matrices is implemented as $\vec{\tau} \rightarrow \hat{U}^\dagger \vec{\tau} \hat{U}$. By \mathcal{K} we denote the complex conjugation operator.

	E	C_4^\pm	C_2	$\Sigma_v^{x(y)}$	$\Sigma_d^{1(2)}$	$\hat{\Delta}_{\mathbf{k}}$
A_1	1	1	1	1	1	$g_{\mathbf{k}}^{A_1} t^0 - g_{\mathbf{k}}^{E,y} t^1 + g_{\mathbf{k}}^{E,x} t^2$
A_2	1	1	1	-1	-1	$g_{\mathbf{k}}^{A_2} t^0 + g_{\mathbf{k}}^{E,x} t^1 + g_{\mathbf{k}}^{E,y} t^2$
B_1	1	-1	1	1	-1	$g_{\mathbf{k}}^{B_1} t^0 + g_{\mathbf{k}}^{E,y} t^1 + g_{\mathbf{k}}^{E,x} t^2$
B_2	1	-1	1	-1	1	$g_{\mathbf{k}}^{B_2} t^0 + g_{\mathbf{k}}^{E,x} t^1 - g_{\mathbf{k}}^{E,y} t^2$
E	$\begin{pmatrix} 1 & 0 \\ 0 & 1 \end{pmatrix}$	$\begin{pmatrix} 0 & \pm 1 \\ \mp 1 & 0 \end{pmatrix}$	$\begin{pmatrix} -1 & 0 \\ 0 & -1 \end{pmatrix}$	$\begin{pmatrix} \pm 1 & 0 \\ 0 & \mp 1 \end{pmatrix}$	$\begin{pmatrix} 0 & \pm 1 \\ \pm 1 & 0 \end{pmatrix}$	$(g_{\mathbf{k}}^{E,x} t^3, g_{\mathbf{k}}^{E,y} t^3)$

Table SII. Transformation properties of the irreps under the action of the spin-lattice symmetry group. In the two-dimensional irrep E the transformation matrices depend on the basis choice. In the last column, we show the form of the gap function in each irrep. The functions $g_{\mathbf{k}}^{A_1}$, $g_{\mathbf{k}}^{A_2}$, $g_{\mathbf{k}}^{B_1}$ and $g_{\mathbf{k}}^{B_2}$ are irreps of the sole C_{4v} , while $g_{\mathbf{k}}^{E,x}$ and $g_{\mathbf{k}}^{E,y}$ are a basis of the two-dimensional irrep E of C_{4v} chosen such that they transform under C_{4v} as shown in the last line of the table. The lowest harmonic contributions for these functions are listed in Table SIII.

SII. SYMMETRY CLASSIFICATION OF THE SUPERCONDUCTING STATES

The symmetry classification of the superconducting symmetries relies on the symmetry group of the Hamiltonian (1). Because of the Rashba spin-orbit coupling, the lattice point group C_{4v} does not leave the Hamiltonian invariant. We have therefore to consider a different group that combines C_{4v} with spin rotations. This group can be simply obtained from the square lattice point group by adding to each of its elements a spin transformation that leaves the Rashba term $\sim (-\sin k_y \tau^1 + \sin k_x \tau^2)$ invariant. In Table SI we list all the discrete combined spin-lattice transformations that leave the Hamiltonian (1) invariant. These symmetries form a discrete group with eight elements $\{E, C_4^+, C_4^-, C_2, \Sigma_v^x, \Sigma_v^y, \Sigma_d^1, \Sigma_d^2\}$. Since this group is equivalent to the point group C_{4v} , its irreducible representations (irreps) are the same: four are one-dimensional (A_1, A_2, B_1, B_2), and one two-dimensional (E). We can therefore classify the symmetry of the superconducting gap according to these irreps. We decompose the gap into form factors

$g_{\mathbf{k}}^{A_1}$	$1, \cos k_x + \cos k_y, 2 \cos k_x \cos k_y, \cos(2k_x) + \cos(2k_y), \dots$
$g_{\mathbf{k}}^{A_2}$	$2\sqrt{2}(\cos k_x - \cos k_y) \sin k_x \sin k_y, \dots$
$g_{\mathbf{k}}^{B_1}$	$\cos k_x - \cos k_y, \cos(2k_x) - \cos(2k_y), \dots$
$g_{\mathbf{k}}^{B_2}$	$2 \sin k_x \sin k_y, 2\sqrt{2}(\cos k_x + \cos k_y) \sin k_x \sin k_y, \dots$
$(g_{\mathbf{k}}^{E,x}, g_{\mathbf{k}}^{E,y})$	$(\sqrt{2} \sin k_x, \sqrt{2} \sin k_y), (2 \cos k_y \sin k_x, 2 \cos k_x \sin k_y), \dots$

Table SIII. Lowest harmonics for the functions $g_{\mathbf{k}}^{A_1}, g_{\mathbf{k}}^{A_2}, g_{\mathbf{k}}^{B_1}, g_{\mathbf{k}}^{B_2}, g_{\mathbf{k}}^{E,x}, g_{\mathbf{k}}^{E,y}$ shown in Table SII. Note that we have employed the normalization convention $\int_{\mathbf{k}} |g_{\mathbf{k}}^X|^2 = 1$.

and t^α matrices, according to Eq. (S24). We notice that the action of the group on the matrices t^α is given by

$$t^\alpha \rightarrow \hat{U}^\dagger t^\alpha \hat{U}^*, \quad (\text{S28})$$

with the different transformation matrices \hat{U} listed in Table SI. As a consequence, when $\alpha = 1, 2, 3$, the matrices t^α transform exactly as the Pauli matrices (as shown in Table SI), while t^0 transforms always trivially. We also remark that, in order to preserve the overall antisymmetry of the pairing wavefunction, the singlet (triplet) components of the gap function Δ_ℓ^α , corresponding to $\alpha = 0$ ($\alpha = 1, 2, 3$), must be symmetric (antisymmetric) for $\mathbf{k} \rightarrow -\mathbf{k}$. For this reason, only the pairs of indices (α, ℓ) with $\alpha = 0$ and $f_{\mathbf{k}}^\ell$ even or $\alpha = 1, 2, 3$ and $f_{\mathbf{k}}^\ell$ odd are allowed in Δ_ℓ^α . In Table SII, we list the irreps of the combined lattice-spin discrete symmetry group, together with the typical form that the gap function $\hat{\Delta}_{\mathbf{k}}$ takes in each one of them. In Table SIII we show the lowest harmonics for the functional dependence of $\hat{\Delta}_{\mathbf{k}}$ on \mathbf{k} . Note that equal spin triplet pairing (described with the matrices t^1 and t^2) can only occur in combination with singlet pairing (described by t^0) in a one-dimensional representation. On the other hand, opposite spin triplet pairing (t^3) can take place only in the two-dimensional irrep E .

SIII. REAL SPACE RENORMALIZED MEAN-FIELD

In Sec. SIB, we solve the renormalized mean-field Hamiltonian in momentum space due to a translational invariance. In this section, we give the details of solving the renormalized mean-field Hamiltonian in real space. In the absence of any inhomogeneities, the two approaches are analogues and give the same results. However, inhomogeneities arising either due to edges/surfaces or disorder can only be captured in a real space picture. Here, we ignore any disorder and focus on the edge properties and possible symmetry breakings within the real space picture. We decouple H_U in Eq. (1) only in the Cooper channel and the resultant real space Hamiltonian is,

$$H_{\text{eff}} = H_0 + \sum_{\substack{i\mu \\ \sigma\sigma'}} \Delta_\mu^{\sigma\sigma'}(i) c_{i+\mu, \sigma'}^\dagger c_{i, \sigma}^\dagger + \text{H.c.}, \quad (\text{S29})$$

where μ denotes the nearest neighbor bonds $\pm x, \pm y$ of the lattice site i , H_0 is defined in Eq. (1) and $\Delta_\mu^{\sigma\sigma'}$ is the superconducting order parameter given by

$$\Delta_\mu^{\sigma\sigma'}(i) = \sum_{s, s'} \sum_{\nu} \tilde{V}_{\mu\nu}^{\sigma\sigma' ss'} \langle c_{i, s} c_{i+\nu, s'} \rangle, \quad (\text{S30})$$

where the interaction strengths are

$$\tilde{V}_{\mu\nu}^{\sigma\sigma' ss'} = \frac{1}{2} \sum_{\alpha\beta} \sum_{\ell\ell'} \tilde{V}_{\ell\ell'}^{\alpha\beta} t_{\sigma\sigma'}^\alpha (t_{ss'}^\beta)^\dagger f^\ell(\mu) [f^{\ell'}(\nu)]^*, \quad (\text{S31})$$

with $f^\ell(\mu)$ being the Fourier transform of $f_{\mathbf{k}}^\ell$ and $\tilde{V}_{\ell\ell'}^{\alpha\beta}$ are obtained from the fRG calculation. H_{MF} is diagonalized using the Bogoliubov-de Gennes transformations [75], $c_{i\sigma} = \sum_n (\gamma_n u_{i\sigma}^n - \sigma \gamma_n^\dagger v_{i\sigma}^{n*})$, where $\gamma_{n\sigma}^\dagger$ ($\gamma_{n\sigma}$) are the creation

(annihilation) operators of the Bogoliubov quasiparticle at a state n , and $u_{i\sigma}^n$ and $v_{i\sigma}^n$ the eigenfunctions with eigenvalues E . The resulting eigen-system is then solved self-consistently for the superconducting order parameters $\Delta_{\mu}^{\sigma\sigma'}$. Moreover, the findings of the order parameters obtained in the momentum space suggest that the dominant pairing is only on nearest neighbors, i.e., either A_1 or B_1 phases, for most parts of the phase diagram except in a narrow region of the phase diagram (B_2 phase red region in Fig. 1). Hence, we restrict the order parameters only to nearest neighbors in real space, as already expressed in Eq. (S29). This helps to reduce the number of independent self-consistent order parameters to 16 per lattice site. We then project local $\Delta_{\mu}^{\sigma\sigma'}$ on onsite equivalents of different pairing components to analyse the symmetry of the order parameter. As shown in Tables. SII and SIII, the only possible nearest neighbour singlet components are d -wave and extended s -wave order parameters. The onsite equivalents of the singlets are given as

$$\Delta_{d/s}(i) = \frac{1}{8} \sum_{\mu} \epsilon_{\mu}^{d/s} \sum_{\sigma} \text{sgn}(\sigma) \Delta_{\mu}^{\sigma\bar{\sigma}}(i), \quad (\text{S32})$$

where Δ_d is the d -wave order parameter, which in momentum space is proportional to $(\cos k_x - \cos k_y)$. Δ_s is the extended s -wave order parameter, which in momentum space is proportional to $(\cos k_x + \cos k_y)$. The prefactor $\epsilon_{\mu}^{d/s}$ is $\epsilon_{\mu}^{d/s} = 1$ for $\mu = \pm x$ and $\epsilon_{\mu}^{d/s} = -1/1$ for $\mu = \pm y$. The phase of the d -wave order parameter is characterized with θ with the definition $\Delta_d(i) = |\Delta_d(i)| \exp(i\theta)$. The triplet order parameters are mainly p -wave with the onsite equivalent given as

$$\Delta_{p_{\nu}}^{\sigma\sigma'}(i) = \frac{1}{2i} \sum_{\mu} \text{sgn}(\mu) \Delta_{\mu}^{\sigma\sigma'}, \quad (\text{S33})$$

where $\Delta_{p_x/p_y}^{\sigma\sigma'}$ are the p -wave order parameters, which in momentum space is proportional to $\sin k_x$ or $\sin k_y$. Different spin components of the p -wave order parameters can be combined to obtain the order parameters in the irreducible representations as

$$\Delta_{A_1}^t(i) = \frac{1}{4} \left(\sum_{\sigma} \text{sgn}(\sigma) \Delta_{p_y}^{\sigma\sigma} - i \sum_{\sigma} \Delta_{p_x}^{\sigma\sigma} \right), \quad (\text{S34})$$

$$\Delta_{B_1}^t(i) = \frac{1}{4} \left(\sum_{\sigma} \text{sgn}(\sigma) \Delta_{p_y}^{\sigma\sigma} + i \sum_{\sigma} \Delta_{p_x}^{\sigma\sigma} \right). \quad (\text{S35})$$

Other mixed-spin triplet components are negligible compared to the equal spin triplets.

The interaction strengths $\tilde{V}_{\mu\nu}^{\sigma\sigma' ss'}$ obtained from fRG give rise to very small values of the superconducting order parameters in most parts of the phase diagram. As a result, the corresponding coherence lengths are large giving the necessity of working with extremely large system sizes to avoid interference effects of the edges while studying the topological edge states. Hence, we scale the interaction strengths obtained from fRG by 10 in order to solve the gap equation Eq. (S30) in real space for all representative points in the phase diagram investigated. We have verified that the qualitative features do not change with reducing the scale factor. We first match the self-consistent superconducting order parameters with periodic boundary condition using the solutions of the momentum space and real space gap equations. We then use open boundary conditions to investigate each of the phases. The choice of the geometry of the boundary depends on the characteristic edge states of different superconducting phases, as explained in the main text.

SIV. EFFECTIVE MODEL AROUND VAN HOVE SINGULARITY POINTS

In this section we derive low-energy Hamiltonians near the two VHS points of the square lattice and discuss the logarithmic divergences in the DOS near these VHSs. The non-interacting Hamiltonian matrix of the Rashba model on the square lattice is given by

$$h(\mathbf{k}) = (\epsilon_{\mathbf{k}} - \mu)\tau_0 + \lambda \vec{g}_{\mathbf{k}} \cdot \vec{\tau}, \quad (\text{S36})$$

where $\epsilon_{\mathbf{k}} = -2t(\cos k_x + \cos k_y) - 4t' \cos k_x \cos k_y$ and $\vec{g}_{\mathbf{k}} = 2t(-\sin k_y, \sin k_x, 0)$. The eigenvalues are $E_{\mathbf{k}} = (\epsilon_{\mathbf{k}} - \mu) \pm 2t\lambda\sqrt{\sin^2 k_x + \sin^2 k_y}$. The chemical potentials of the two VHS points are $\mu_{\text{VHS}} = \pm 2(\sqrt{(t \pm 2t')^2 + t^2\lambda^2} - t)$. The

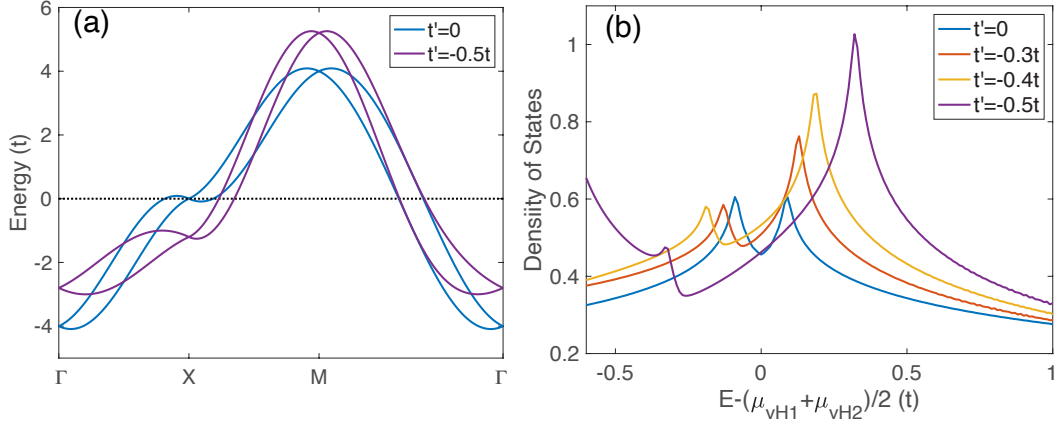


Figure S1. Band structures (a) and density of states (DOS) (b) around two the VHSs of the square lattice as a function of the second neighbor hopping t' .

low-energy Hamiltonian around the VHS point $(k_c, 0)$ on the $\Gamma - X$ direction (VHS1) reads

$$\begin{aligned} \epsilon(k_c + q_x, q_y) &= -2[(\cos k_c - \sin k_c \lambda + 1) + 2 \cos k_c t'] + q_x^2 [t(\cos k_c - \sin k_c \lambda) + 2 \cos k_c t'] \\ &\quad + q_y^2 \left(2 \cos k_c t' + \frac{|\lambda|t}{\sin k_c} + t \right), \\ &= -2[t(\cos k_c - \sin k_c \lambda + 1) + 2 \cos k_c t'] - q_x^2 \sin k_c \frac{(t + 2t')^2 + t^2 \lambda^2}{\lambda t} + q_y^2 \frac{2 \sin k_c \cos k_c t' + t \sin k_c + |\lambda|t}{\sin k_c}, \end{aligned} \quad (\text{S37})$$

where k_c is given by $\tan k_c = -\frac{\lambda t}{t + 2t'}$. The dispersion can be further simplified to

$$\epsilon(k_c + q_x, q_y) = 2(D_1 - t) - q_x^2 D_1 + q_y^2 \left[-\frac{2(t + 2t')t'}{D_1} + D_1 + t \right], \quad (\text{S38})$$

with $D_1 = \sqrt{(t + 2t')^2 + \lambda^2 t^2}$.

The low-energy Hamiltonian around the VHS point (π, k'_c) on the $X - M$ direction (VHS2) reads

$$\begin{aligned} \epsilon(\pi + q_x, k'_c + q_y) &= 2[t(-\cos k'_c - \sin k_c \lambda + 1) + 2 \cos k'_c t'] + q_y^2 [t(\cos k'_c + \sin k'_c \lambda) - 2 \cos k'_c t'] \\ &\quad - q_x^2 \left(2 \cos k'_c t' + \frac{|\lambda|t}{\sin k'_c} + t \right) \\ &= 2[t(-\cos k'_c - \sin k_c \lambda + 1) + 2 \cos k'_c t'] + q_y^2 \sin k_c \frac{(t - 2t')^2 + t^2 \lambda^2}{\lambda t} \\ &\quad - q_x^2 \left(2 \cos k'_c t' + \frac{|\lambda|t}{\sin k'_c} + t \right), \end{aligned} \quad (\text{S39})$$

where k'_c is given by $\tan k'_c = \frac{\lambda t}{t - 2t'}$. The dispersion can be further simplified to

$$\epsilon(\pi + q_x, q_y) = -2(D_2 - t) + q_y^2 D_2 - q_x^2 \left[\frac{2(t - 2t')t'}{D_2} + D_2 + t \right], \quad (\text{S40})$$

with $D_2 = \sqrt{(t - 2t')^2 + \lambda^2 t^2}$. The two VHSs are derived from the saddle at the X/Y point with Rashba spin-orbit coupling. In the absence of the next-nearest hopping t' , the dispersion around these two VHSs are similar and the corresponding effective masses along x and y are the same, leading to the same divergent density of states (see blue curves in Fig. S1). With increasing $|t'|$ (negative t'), the VHS1 on the $\Gamma - X$ line rapidly moves away from the X point, while the VHS2 on the $X - M$ line slightly move closer to the X point. As the coefficient of the logarithmically divergent DOS is proportional to $\sqrt{m_x m_y}$, where $m_{x/y}$ is the effective mass along x/y direction, this will make the DOS around the two VHSs different, which can be seen in Fig. S1. The saddle points on the $X - M$ lines (VHS2) are close to the X point and this will generate strong ferromagnetic spin fluctuations, which promoting spin-triplet pairing. This explains the dominant spin-triplet pairing near the VHS2 filling ($|t'| > 0.3$) in our fRG calculations.

SV. TOPOLOGICAL EDGE AND CORNER STATES

In this section we study the topological edge and corner states of the A_1 and $A_1 + iB_1$ superconducting phases. With the spinor $\Psi_{\mathbf{k}} = (c_{\mathbf{k}\uparrow}^\dagger, c_{\mathbf{k}\downarrow}^\dagger, c_{-\mathbf{k}\uparrow}, c_{\mathbf{k}\downarrow})$ the BdG Hamiltonian can be written as $\mathcal{H}_{\text{BdG}} = \sum_{\mathbf{k}} \Psi_{\mathbf{k}}^\dagger H_{\text{BdG}}(\mathbf{k}) \Psi_{\mathbf{k}}$ with the Hamiltonian matrix

$$H_{\text{BdG}}(\mathbf{k}) = \begin{pmatrix} h(\mathbf{k}) & \Delta(\mathbf{k}) \\ \Delta^\dagger(\mathbf{k}) & -h^*(\mathbf{k}) \end{pmatrix}, \quad (\text{S41})$$

where the pairing term is $\Delta(\mathbf{k}) = [\Delta_S(\mathbf{k}) + \Delta_T(\mathbf{k})\vec{d} \cdot \vec{\tau}]i\tau_2$, with $\Delta_S(\Delta_T)$ being the spin-singlet (spin-triplet) pairing component. For the helical p -wave (A_1 pairing state), the pairing matrix is

$$\Delta_T^{A_1} \vec{d} = \Delta_p(-\sin k_y, \sin k_x), \quad (\text{S42})$$

with \vec{d} being parallel to \vec{g} ($\vec{d}_{\mathbf{k}} \parallel \vec{g}_{\mathbf{k}}$). The singlet pairing component is

$$\Delta_S(\mathbf{k}) = \Delta_0 + \Delta_s(\mathbf{k}) + \Delta_d(\mathbf{k}) = \Delta_0 + \Delta_s(\cos k_x + \cos k_y) + \Delta_d(\cos k_x - \cos k_y). \quad (\text{S43})$$

The BdG Hamiltonian can be written as,

$$H_{\text{BdG}}(\mathbf{k}) = \epsilon_{\mathbf{k}}\eta_z\tau_0 + g_x(\mathbf{k})\eta_0\tau_x + g_y(\mathbf{k})\eta_z\tau_y - \Delta_p[d_x(\mathbf{k})\eta_x\tau_z + d_y(\mathbf{k})\eta_y\tau_z] - \Delta_S(\mathbf{k})\eta_y\tau_y, \quad (\text{S44})$$

where $\vec{\eta}$ and $\vec{\tau}$ are Pauli matrices in the Nambu and spin space, respectively. This Hamiltonian has time-reversal symmetry, particle-hole symmetry and chiral symmetry, satisfying $\mathcal{T}H_{\text{BdG}}(\mathbf{k})\mathcal{T}^{-1} = H_{\text{BdG}}(-\mathbf{k})$ with $\mathcal{T} = i\tau_2\mathcal{K}$, $\mathcal{C}H_{\text{BdG}}(\mathbf{k})\mathcal{C}^{-1} = -H_{\text{BdG}}(-\mathbf{k})$ with $\mathcal{C} = \eta_1\mathcal{K}$ and $\mathcal{S}H_{\text{BdG}}(\mathbf{k})\mathcal{S}^{-1} = -H_{\text{BdG}}(\mathbf{k})$ with $\mathcal{S} = \mathcal{T}\mathcal{C} = i\eta_1\tau_2$. Owing to $\mathcal{T}^2 = -1$, $\mathcal{C}^2 = +1$ and $\mathcal{S}^2 = 1$, the system belongs to the DIII class of topological superconductors [3] and is characterized by a \mathbb{Z}_2 invariant in two dimensions [76].

To study the edge states, we expand the above model around the Γ point. (The expansion around the M point is briefly discussed at the end.) The effective model around the Γ point reads,

$$H_{\text{BdG}}^\Gamma(\mathbf{q}) = [M_0 + B(q_x^2 + q_y^2)]\eta_z\tau_0 - Aq_y\eta_0\tau_x + Aq_x\eta_z\tau_y - \Delta_p(-q_y\eta_x\tau_z + q_x\eta_y\tau_z) - \Delta_S(\mathbf{q})\eta_y\tau_y. \quad (\text{S45})$$

Here, the parameters are given by

$$\begin{aligned} M_0 &= -4t - 4t' - \mu, & B &= t + 2t', & A &= t\lambda, \\ \text{and } \Delta_S &= \Delta_0 + 2\Delta_s + \frac{1}{2}\Delta_s(q_x^2 + q_y^2) + \frac{1}{2}\Delta_d(q_x^2 - q_y^2). \end{aligned} \quad (\text{S46})$$

We first omit the singlet pairing and study the topological edge states for the helical p -wave pairing. Considering open boundary conditions along the x direction, we let $q_x \rightarrow -i\partial_x$ in the Hamiltonian (S45) and obtain

$$\begin{aligned} H_{\text{BdG}}^\Gamma(-i\partial_x, q_y) &= H_0^\Gamma(-i\partial_x, q_y) + H_1^\Gamma(-i\partial_x, q_y), \\ H_0^\Gamma(-i\partial_x, q_y) &= (M_0 - B\partial_x^2)\eta_z\tau_0 - iA\eta_z\tau_y\partial_x + \Delta_p\eta_y\tau_0\partial_x, \\ H_1^\Gamma(-i\partial_x, q_y) &= -Aq_y\eta_0\tau_x + \Delta_p q_y\eta_x\tau_z, \end{aligned} \quad (\text{S47})$$

where we keep the dominant linear q_y terms but neglect the insignificant q_y^2 terms. In the following, we solve the Hamiltonian $H_0^\Gamma(-i\partial_x, q_y)$ and treat $H_1^\Gamma(-i\partial_x, q_y)$ perturbatively. As the system belongs to DIII class, zero-energy localized edge modes will appear in the topologically nontrivial regime. The eigenvalue equation for these zero modes reads $H_0^\Gamma(-i\partial_x, q_y)\psi(x) = 0$ with the boundary condition $\psi(0) = \psi(+\infty) = 0$. With the wavefunction ansatz $\psi(x) = e^{-\alpha x}\phi$, the eigenvalue equation is further simplified to

$$[(M_0 - B\alpha^2)\eta_z\tau_0 + iA\alpha\eta_z\tau_y - i\Delta_p\alpha\eta_y\tau_0]\phi = 0. \quad (\text{S48})$$

By multiplying $\eta_z\tau_0$ from the right hand side, the above equation can be brought into the form

$$[(M_0 - B\alpha^2) + iA\alpha\tau_y - \Delta_p\alpha\eta_x]\phi = 0. \quad (\text{S49})$$

Therefore, the four-component wavefunction ϕ is an eigenstate of both σ_y and η_x , and the corresponding eigenbasis is

$$\begin{aligned} \phi_1 &= |\eta_x = 1\rangle \otimes |\tau_y = 1\rangle, \\ \phi_2 &= |\eta_x = 1\rangle \otimes |\tau_y = -1\rangle, \\ \phi_3 &= |\eta_x = -1\rangle \otimes |\tau_y = 1\rangle, \\ \phi_4 &= |\eta_x = -1\rangle \otimes |\tau_y = -1\rangle. \end{aligned} \quad (\text{S50})$$

For the four ϕ_i of the eigenbasis we obtain the equation $B\alpha^2 + (-iAf_\sigma^i + \Delta_p f_\eta^i)\alpha - M_0 = 0$, with $f_{\sigma/\eta}^i = \pm$, which has the following roots

$$\alpha_{1,2} = \frac{(-\Delta_p f_\eta^i + iAf_\sigma^i) \pm \sqrt{(-\Delta_p f_\eta^i + iAf_\sigma^i)^2 + 4BM_0}}{2B}. \quad (\text{S51})$$

The boundary condition $\psi(+\infty) = 0$ implies $\text{Re}(\alpha) > 0$. With $\alpha_1 + \alpha_2 = (-\Delta_p f_\eta^i + iAf_\sigma^i)/B$ and taking $A, B > 0$, only $\phi_{3,4}$ satisfies the above constrain with $f_\eta^i = -1$. As the pairing potential Δ_p is small, we omit A^2/B^2 and A/B^2 terms in the following calculations. With including the boundary condition $\psi(0) = 0$, the two wavefunctions can be written as

$$\psi_{3/4}(x) = \mathcal{N}_0 e^{-\beta_0 x} e^{\mp i\beta_1 x} \sin(\beta_2 x) \phi_{3/4}, \quad (\text{S52})$$

with $\beta_0 = \Delta_p/2B$, $\beta_1 = A/2B$, $\beta_2 = \sqrt{-4BM_0 + A^2}/2B$ and $\mathcal{N}_0 = \sqrt{\frac{4\beta_0(\beta_0^2 + \beta_2^2)}{\beta_2^2}}$. In the basis of $\psi_{3,4}(x)$, the elements of $H_1^\Gamma(-i\partial_x, q_y)$ can be written as

$$\begin{aligned} \langle \psi_3 | H_1^\Gamma(-i\partial_x, q_y) | \psi_3 \rangle &= \langle \psi_4 | H_1^\Gamma(-i\partial_x, q_y) | \psi_4 \rangle = 0, \\ \langle \psi_3 | H_1^\Gamma(-i\partial_x, q_y) | \psi_4 \rangle &= \mathcal{N}_1 (A - i\Delta_p) q_y, \\ \langle \psi_4 | H_1^\Gamma(-i\partial_x, q_y) | \psi_3 \rangle &= \mathcal{N}_1 (A + i\Delta_p) q_y, \end{aligned} \quad (\text{S53})$$

with the factor $\mathcal{N}_1 = \frac{\Delta_p}{A} (1 - \frac{A^2}{4BM_0})$. Here, we used $\tau_x|\tau_y = \pm 1\rangle = \pm i|\tau_y = \mp 1\rangle$ and $\tau_z|\tau_y = \pm 1\rangle = |\tau_y = \mp 1\rangle$. Therefore, the effective Hamiltonian of the helical edge states reads

$$\tilde{H}_1^\Gamma(q_y) = \mathcal{N}_1 (Aq_y s_x - \Delta_p q_y s_y), \quad (\text{S54})$$

with \mathbf{s} being the Pauli matrices in the $\psi_{3,4}(x)$ space. The bulk topological invariant can be directly calculated using Ref. [58]. For the used parameter setting $t = 1, t' = -0.5, \mu = -1.6$, there are four Fermi surfaces: the pockets around Γ and X/Y points are attributed to the positive helicity (+) band and the pocket around the M point is attributed to the negative helicity (-) band. As the pairing potential for the pockets around Γ and M changes sign, the system is \mathbb{Z}_2 topologically nontrivial according to $N_{2D} = \Pi_s [\text{sgn}(\Delta_s)]^{m_s}$ [58] and the Dirac cone in the edge states should be located at the projection of the M point, namely \bar{X}/\bar{Y} in the 1D edge Brillouin zone.

Next, we consider the spin-singlet pairing perturbation $H_2^\Gamma = \Delta_s(\mathbf{q})\eta_y\tau_y$ with a real gap. It can be easily shown that this perturbation cannot gap out the edge states. Then we consider the iB_1 pairing perturbation $H_3^\Gamma(\mathbf{q}) = \frac{1}{2}\Delta_d(q_x^2 - q_y^2)\eta_x\tau_y$, which breaks time-reversal symmetry. With open boundary conditions in the x direction, we replace q_x by the momentum operator and obtain $H_3^\Gamma(\mathbf{q}) = -\frac{1}{2}\Delta_d(\partial_x^2 + q_y^2)\eta_x\tau_y$. Projecting this into the basis of $\psi_{3/4}(x)$ gives

$$\tilde{H}_3^\Gamma(q_y) = -\frac{\mathcal{N}_2\Delta_d}{2}s_z, \quad (\text{S55})$$

with $\mathcal{N}_2 = \frac{A^2 - 4BM_0}{2B}$. Thus, the time-reversal breaking iB_1 pairing introduces a mass term for the edge states. Moreover, we find that the mass term changes sign between the x -terminated and y -terminated edges, due to the d -wave pairing nature. Hence, the edge Hamiltonians on the x - and y -terminated edges are given by

$$\tilde{H}_x^\Gamma(q_y) = \mathcal{N}_1 (Aq_y s_x - \Delta_p q_y s_y) - \frac{\mathcal{N}_2\Delta_d}{2}s_z, \quad (\text{S56})$$

$$\tilde{H}_y^\Gamma(q_x) = \mathcal{N}_1 (Aq_x s_x - \Delta_p q_x s_y) + \frac{\mathcal{N}_2\Delta_d}{2}s_z, \quad (\text{S57})$$

respectively. When these two edges meet at a corner, the mass term must go through zero. As a consequence, a Majorana zero-energy state appears at the corner, indicating higher-order topological superconductivity.

Expanding the BdG Hamiltonian (S44) around the M point, we obtain an expression of the same form as Eq. (S45) but with the modified parameters

$$\begin{aligned} M_0 &= 4t - 4t' - \mu, \\ B &= -t + 2t', \\ A &= -t\lambda. \end{aligned} \quad (\text{S58})$$

With our parameter choices for t, t' and λ , $B < 0$ and $A < 0$ but $AB > 0$ still holds. Therefore, the wavefunctions and the corresponding edge Hamiltonians remain similar. Therefore, Majorana corner modes still appear.

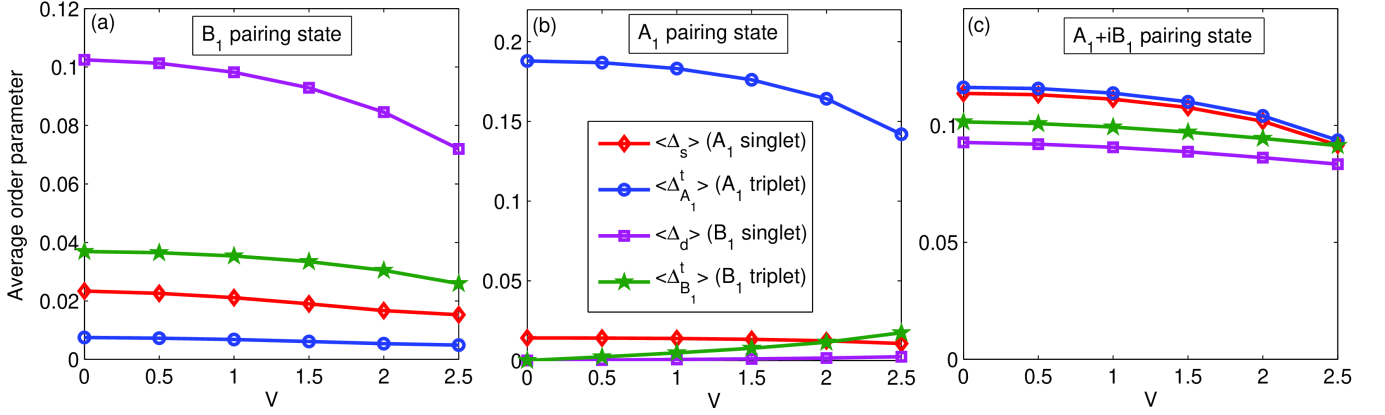


Figure S2. Dependence of average order parameter magnitudes as a function of disorder strength V for three representative points of the phase diagram, (a) $\mu = -0.5$ and $t' = -0.5$ (cross I in Fig. 1 of the main text), (b) $\mu = -1.6$ and $t' = -0.5$ (cross III in Fig. 1 of the main text), and (c) $\mu = -1.2$ and $t' = -0.5$ (cross II in Fig. 1 of the main text). V is expressed in units of t .

SVI. DISORDER EFFECTS ON THE SUPERCONDUCTING STATES

Here we study the disorder effects of the three different kinds of topological superconducting states obtained in the phase diagram shown in Fig. 1 of the main text. We introduce non-magnetic chemical potential disorder by adding a term $H_V = \sum_i V_i n_i$ to the Hamiltonian with the disordered Hamiltonian given by $H_{\text{dis}} = H_{\text{eff}} + H_V$ where H_{eff} is given in Eq. (S29) and V_i is a site-dependent non-magnetic impurity potential drawn from a random distribution, such that $V_i \in [-V/2, V/2]$ uniformly, also commonly known as Anderson disorder. With the new method of fRG+MFT developed in this paper, we can now investigate the disorder effects of the different superconducting phases. Using the same method as in Sec. SIII, we self-consistently solve for all the order parameters with periodic boundary conditions in a 30×30 lattice. In the presence of disorder, all the order parameters vary at every site. Hence to quantify the average superconducting properties, we define average of the order parameter magnitudes as $\langle \Delta_{s/d} \rangle = 1/N \sum_i |\Delta_{s/d}|$ and $\langle \Delta_{A_1/B_1}^t \rangle = 1/N \sum_i |\Delta_{A_1/B_1}^t|$ with the site-dependent order parameters given by the definitions in Eq. (S32) and Eq. (S33). In Fig. S2, we show the disorder-dependence of average order parameter magnitudes for three representative points of the phase diagram marked by three crosses in Fig. 1 of the main text with different dominant superconducting instabilities. For $V = 0$ the dominant instabilities are clearly visible in (a) and (b): for B_1 pairing state it is the singlet Δ_d and for A_1 pairing state it is the $\Delta_{A_1}^t$. In (c), the coexistence of B_1 and A_1 pairing states is also apparent with all the order parameters being comparable in magnitude. With increasing disorder, there is a reduction in the dominant order parameters. However, the dominant orders survive with considerable magnitudes even upto $V = 2.5$ for all the three cases making them quite robust to disorder. Since the computational cost increases in the presence of disorder, the disorder effect on the whole phase diagram is left for a future work. We have also verified that the edge properties of all three topological state do not change atleast for $V \leq 2.5$. The results in this section are only presented for a single configuration of disorder. We do not expect the disorder-dependence of the order parameters to change after disorder averaging.